AFRL-AFOSR-VA-TR-2019-0244

Vortex Dynamics & Boundary Layer Characteristics of Airfoils with Surface Modifications

Isaac Choutapalli
University of Texas- Rio Grande Valley

08/16/2019
Final Report

Air Force Research Laboratory
AF Office Of Scientific Research (AFOSR)/ RTA1
Arlington, Virginia 22203
Air Force Materiel Command

DISTRIBUTION A: Distribution approved for public release.

REPORT DOCUMENTATION PAGE

Form Approved
OMB No. 0704-0188

1. REPORT DATE *(DD-MM-YYYY)*	2. REPORT TYPE	3. DATES COVERED *(From - To)*
19-08-2019	Final Performance	15 Jul 2014 to 14 Jul 2018

4. TITLE AND SUBTITLE
Vortex Dynamics & Boundary Layer Characteristics of Airfoils with Surface Modifications

5a. CONTRACT NUMBER

5b. GRANT NUMBER
FA9550-14-1-0199

5c. PROGRAM ELEMENT NUMBER
61102F

6. AUTHOR(S)
Isaac Choutapalli

5d. PROJECT NUMBER

5e. TASK NUMBER

5f. WORK UNIT NUMBER

7. PERFORMING ORGANIZATION NAME(S) AND ADDRESS(ES)
University of Texas- Rio Grande Valley
1201 W University Dr
EDINBURG, TX 78539-2909 US

8. PERFORMING ORGANIZATION REPORT NUMBER

9. SPONSORING/MONITORING AGENCY NAME(S) AND ADDRESS(ES)
AF Office of Scientific Research
875 N. Randolph St. Room 3112
Arlington, VA 22203

10. SPONSOR/MONITOR'S ACRONYM(S)
AFRL/AFOSR RTA1

11. SPONSOR/MONITOR'S REPORT NUMBER(S)
AFRL-AFOSR-VA-TR-2019-0244

12. DISTRIBUTION/AVAILABILITY STATEMENT
A DISTRIBUTION UNLIMITED: PB Public Release

13. SUPPLEMENTARY NOTES

14. ABSTRACT

An experimental study is conducted to investigate the aerodynamic and flow field characteristics of a NACA-0010 airfoil with and without leading-edge tubercles in flow with freestream turbulence intensity of 4%. Preliminary measurements of wake velocity profiles, force measurements using a six-component force balance and Particle Image Velocimetry (PIV) flow field measurements were carried out. The measurements were carried out for two types of airfoils, one with smooth leading edge (baseline) and the other with modified leading-edge by introducing tubercles. All the experiments were carried out at Reynolds numbers ranging from 160,000 to 412,000. The results from this study show that in the range of Reynolds numbers tested for the half-span airfoil model, while there is no performance enhancement pre-stall, significant performance enhancement is acheived for stall and post-stall conditions.

15. SUBJECT TERMS
Vortex, Boundary Layer

16. SECURITY CLASSIFICATION OF:			17. LIMITATION OF ABSTRACT	18. NUMBER OF PAGES	19a. NAME OF RESPONSIBLE PERSON
a. REPORT	b. ABSTRACT	c. THIS PAGE			ABATE, GREGG
Unclassified	Unclassified	Unclassified	UU		

Standard Form 298 (Rev. 8/98)
Prescribed by ANSI Std. Z39.18

			19b. TELEPHONE NUMBER *(Include area code)* 703-588-1779

VORTEX DYNAMICS AND BOUNDARY LAYER CHARACTERISTICS OF AIRFOILS WITH SURFACE MODIFICATIONS

AFOSR Award FA9550-14-1-0199

Final Report

PI: Dr. Isaac Choutapalli

The University of Texas – Rio Grande Valley

Department of Mechanical Engineering

Edinburg, TX - 78539

TABLE OF CONTENTS

Summary of Key Results

An experimental study is conducted to investigate the aerodynamic and flow field characteristics of a NACA-0010 airfoil with and without leading-edge tubercles in flow with freestream turbulence intensity of 4%. Preliminary measurements of wake velocity profiles, force measurements using a six-component force balance and Particle Image Velocimetry (PIV) flow field measurements were carried out. The measurements were carried out for two types of airfoils, one with smooth leading edge (baseline) and the other with modified leading-edge by introducing tubercles. All the experiments were carried out at Reynolds numbers ranging from 160,000 to 412,000. The results from this study show that in the range of Reynolds numbers tested for the half-span airfoil model, while there is no performance enhancement pre-stall, significant performance enhancement is acheived for stall and post-stall conditions.

I. Introduction

Every year, billions of gallons of fossil fuel are used to enhance lift and overcome drag encountered by vehicles moving in air or water. Numerous attempts have been made over the past few decades to reduce drag and enhance lift. The methods include turbulent transition delay, reduction of near-wall momentum by injecting fluid normal to the wall, polymer and microbubbles introduction, large-eddy break up devices, riblets (e.g. skin of an alligator with 3D riblet-like structures), complaint surfaces (e.g. dolphin skin), wavy walls and other surface modifications. Moderate reductions in drag of up to 10% were reported in most studies involving flow over lifting surfaces. Miklosovic (2004) studied the aerodynamic characteristics of an airfoil similar to the pectoral fin of a humpback whale. He found that a scaled model of the pectoral fin would provide the optimal lift enhancement with minimum drag penalty. Fish et al. (2011) studied the a two-dimensional airfoil similar to the pectoral fin of a humpback whale. The investigation showed that viscous drag is reduced by nearly 11%, lift increased by 5%, 17% increase in the lift-to-drag ratio and a 40% increase in the stall angle. Murray, Miklosovic, Fish, and Howle (2005) found that tubercles increased aerodynamic performance for all sweep angles investigated for chord Reynolds number of 550,000. Johari

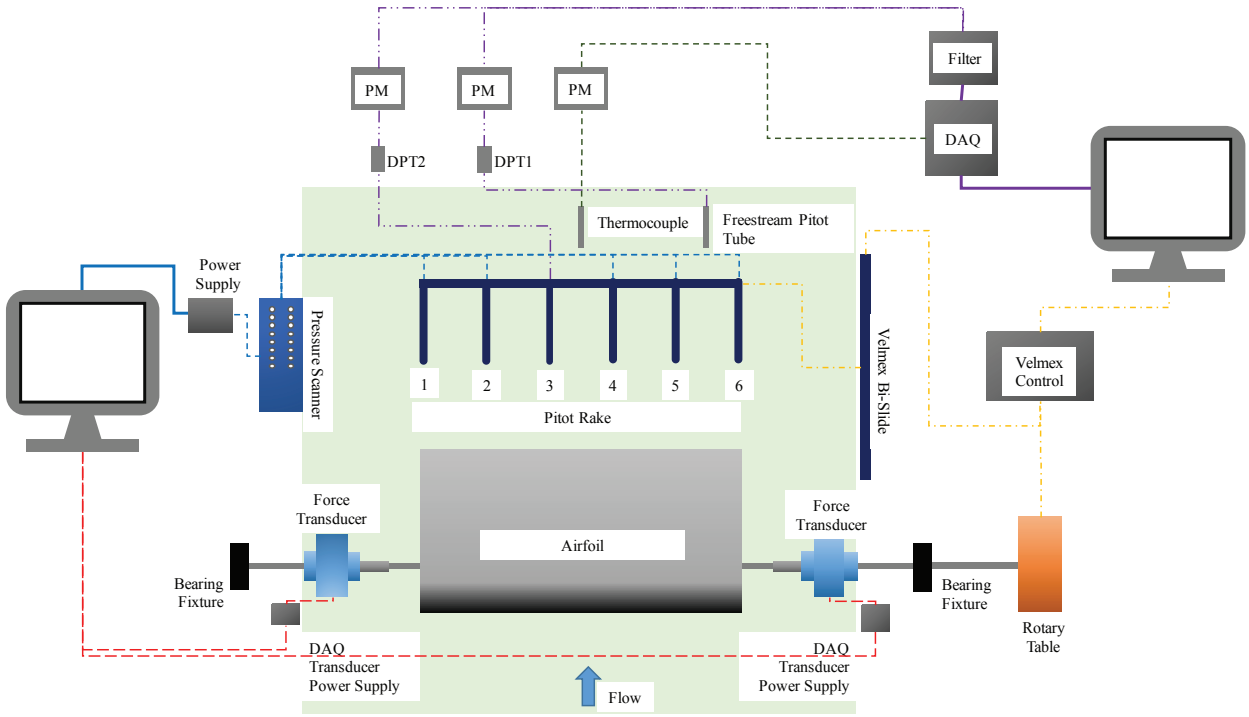

Figure 1. A schematic of the low-speed wind tunnel testing facility.

et. al. (2007) found that for Reynolds number of 180,000, the NACA 63-021 airfoil with tubercles showed decreased performance with respect to both the stall angle and maximum lift coefficient. The investigation by Weber, Howle, and Murray (2010), however, revealed that in the range of Reynolds numbers from 200,000 to 800,000, airfoils with tubercles produced more gradual stall and higher lift post-stall. Investigations by Hansen et. al. (2012) is a function of Reynolds number and less likely a function of three-dimensional effects. However, in most of the studies the effect of freestream turbulence intensity on tubercle performance was not addressed. In this study, preliminary results are presented for tubercle performance in the presence of freestream with high turbulence intensity.

II. Apparatus, Instrumentation and Procedures

A. The Facility

The experiments were carried out in the low-speed wind tunnel facility located in the Aerodynamics and Propulsion Laboratory at the University of Texas - Rio Grande Valley. Figure 2 shows a schematic of the

wind tunnel. The tunnel is an open-circuit subsonic wind tunnel and is driven by a 200hp motor to achieve a test velocity of 40 m/sec (Mach 0.12) by turning an 7-bladed fan driven by a 2:1 speed increaser. The wind tunnel inlet has a honeycomb network followed by a 9:1 contraction to minimize test section turbulence. The test section can accommodate up to an 8% blockage without causing difficulties with obtaining the desired speed in the tunnel. The test section is 2 feet high by 2 feet wide by 4 feet long to provide sufficient space to do meaningful studies with 4% turbulent flow.

The airfoil is mounted in the test section supported by two circular aluminium shafts rigidly connected to two force/torque transducers on each side of the wind tunnel test section wall as shown in the schematic. The transducers are in turn supported by ball bearing fixtures ensuring free rotational motion. This mounting mechanism ensures that all the forces and torque experienced by the airfoil are completely transferred to the transducers. The airfoil which has a span of 6 inches is mounted in such a way that the centerline of the wind tunnel coincides with that of the airfoil. The angle of attack of the airfoil is controlled by a Velmex rotary table with 90:1 gear ratio and a PK245-01AA stepping motor with a resolution of 500 revolutions per degree.

B. Instrumentation

A data acquisition program, written using LABVIEW, was used to record different flow parameters. Different parameters like the stagnation pressure, temperature and load cell readings are monitored and recorded. The data is acquired using a National Instruments PCI-MIO-16E-1 data acquisition card. The primary measurements in this study comprised of wake velocity, force/torque and PIV flow field measurements. The wake velocity measurements were carried out using a six-probe pitot rake attached to a Velmex bi-slide. The two center probes in the rake are connected to Omega PX-409 high stability, low drift differential pressure transducers. These transducers have an accuracy (Linearity, hysteresis and repeatability combined) of ± 0.05 % of the full-scale reading. This corresponds to a measurement error of ± 0.05 psia. Additional uncertainty up to a maximum of 0.024 psia is present due to the data being acquired through analog-to-digital (A/D) card. Hence, the total uncertainty in the pressure measurements is ± 0.074 psia.

The output from the pressure transducers is filtered using a Stanford Research SR640 programmable two-

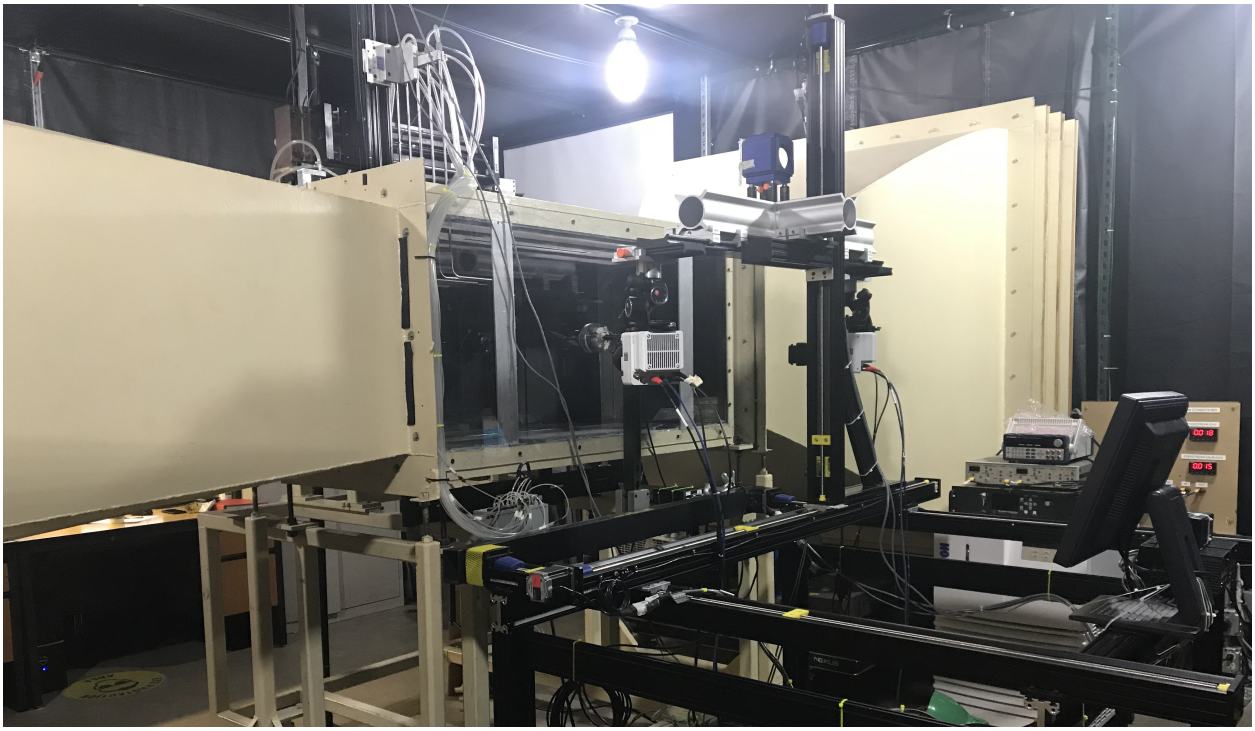

Figure 2. Low-speed wind tunnel testing facility at UTRGV.

channel low pass filter with a 200Hz cut-off. The filter is an 8-pole, 6-zero elliptic-type with 115dB per octave rolloff, 0.1 dB of passband ripple, and 80dB stopband attenuation. The outer probes of the rake are connected to a model 9116 pneumatic intelligent pressure scanner with a system accuracy of up to ±0.05% FS. The vertical traverse of the pitot rake is controlled using a Velmex bi-slide positioning system with a travel length of 30 inches. The forces and torque experienced by the airfoil are measured using two 9105-TIF-DELTA ATI multi-axis force/torque transducers. The transducer has a resolution of 0.0625N for force measurements and 0.000375N-m for torque measurements. The temperature in the test section was monitored by an OMEGA K-type thermocouple. For a maximum temperature of 300K, the total experimental uncertainty is 2.5°C. The signals from these transducers are amplified using a DC amplifier and recorded using a NI PCI-MIO-16E-1 DAQ card. All the transducers were calibrated under static conditions prior to using them in the actual experimental runs.

C. Particle Image Velocimetry (PIV)

The flow field was captured by means of Stereoscopic Particle Image Velocimetry (PIV) measurements using LaVision DaVis-10 software. The illumination is provided by a dual-oscillator digitally sequenced Nd:YAG laser (DM30-527-DH-PIV Photonics laser) with 30 mJ/pulse at 532nm wavelength. The maximum repetition rate for the laser is 10kHz. A light sheet of 1 mm thickness is created by suitable combination of spherical and cylindrical lenses. The images are recorded by two CMOS cameras (Phantom VEO 410L) with a resolution 1280(H) x 800 (V) pixels of a size of 20×20 μm^2. The cameras were fitted with a 105 mm (f/2.8) Nikon lenses. The resulting image area covered by each camera is $6d$ (H) $\times$ $4d$ (V) or 304.8 mm $\times$ 203.2 mm. In the present experiments, 2500 image pairs per second were acquired with time delay between two successive images in a pair being 20 μs. The cameras were positioned at approximately 45 degrees to the flow axis.

The flow was seeded with smoke particles (1-10μm) produced by a Rosco fog generator. A total of 1500 samples obtained from the PIV measurements were processed together to calculate the global mean quantities. Using the central limit theorem (Ott [1], Rohsenow and Choi [2]), the uncertainty (ε) in the PIV measurements can be calculated as $\varepsilon = \sigma/\sqrt{N}$, where σ is the standard deviation of the measured values and N is the number of samples. Based on 95% confidence interval, the uncertainty in the mean velocity is about $\pm 0.5\%$.

Since the flow field, especially during post stall, is dominated by strong flow acceleration and deceleration, it is important to ensure that the seed particles track the flow accurately. In such flow, the buoyancy, dynamic pressure field and the added mass of the seed particles can be neglected since the seed particles are much denser than the ambient air (Hinze [3]). Since the Weber number ($We = \dfrac{d_p \rho_f U^2}{\sigma}$ where d_p is the particle diameter, ρ_f is the density of ambient air, U is the characteristic velocity and σ is the surface tension) based on the seed particle diameter used in this study is small ($We = 0.13$), it can be assumed that the particles are spherical. Neglecting body forces, the particle motion can be approximated by the differential equation

$$\vec{F}_D = m_p \frac{d\vec{u}_p}{dt} \tag{1}$$

Here F_D is the drag force on the particle by the fluid. It is further assumed that the relative Reynolds

number, $Re_p = \frac{\rho_f \left| u_f - u_p \right| d_p}{\mu_f} << 1$. Here the subscript f refers to the fluid which is the ambient air and p refers to the seed particle. The drag force can then be calculated using the Stokes expression

$$\vec{F}_D = 3\pi\mu_f \left| u_f - u_p \right| d_p \tag{2}$$

The dynamic equation of motion hence becomes

$$\left| u_f - u_p \right| = \frac{\rho_p d_p^2 \left| \dot{u_p} \right|}{18\rho_f \nu_f} \tag{3}$$

where ρ_p is the particle density, $\dot{u}_p$ is the total time derivative of the particle velocity, ρ_f is the density of the fluid and ν_f is the kinematic viscosity of the fluid. The details of the derivation of the above expression can be found in Ross [6]. The maximum measured velocity is 40m/s at a vortex shedding frequency of about 50 Hz at a post stall condition of 18^o angle of attack. The velocity at a given point in the stall region can, for sake of simplicity, be assumed as having a sinusoidal variation with time. The sinusoidal dependence in time can be expressed by as $u_p = 40sin(\omega t)$ The maximum acceleration can be estimated by [Mei [7]] $|\dot{u_p}| = |40\omega cos(\omega t)| = 40(2\pi)(50) = 12.6 \times 10^3 m/s^2$. For the ROSCO fog fluid used in the present experiments, the specific gravity of the particle is 1.12 (ROSCO material safety data sheet). Taking the kinematic viscosity of air as $14.7 \times 10^{-6} m^2/s$, it can be inferred from above equation that the seed particle with diameter $0.3\mu m$ will have a maximum 'slip' or 'lag' of 0.0037 m/s. For the maximum velocity of 40 m/s, the maximum error is approximately 0.04%. Furthermore, based on the magnitude of the maximum 'slip' or 'lag', the relative Reynolds number is calculated to be 0.0013. Hence the assumption with regard to the relative Reynolds number holds true ($Re_p << 1$).

Since the flow considered here is dominated by periodic oscillations, it is also essential to ensure that the particles respond faithfully to flow oscillations. The velocities of the seed particles and fluid in the frequency domain can be expressed in terms of Fourier integrals as (Hjelmfelt and Mockros [8]; Prestridge et al. [9])

$$\vec{v}_p(\omega) = \int_{-\infty}^{\infty} \vec{u}_p(\tau) e^{-i\omega\tau} d\tau \tag{4}$$

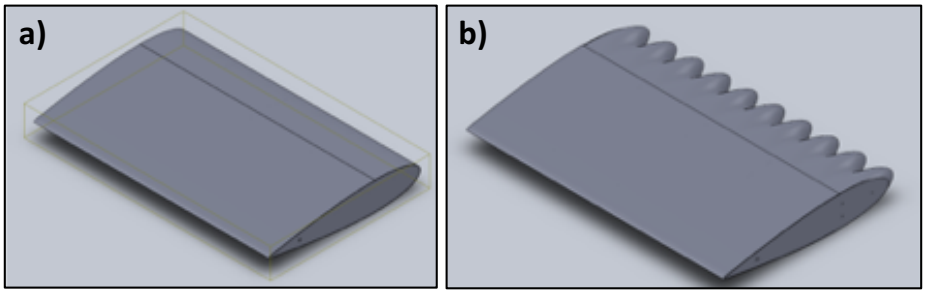

Figure 3. a) NACA 0010 airfoil with smooth leading-edge (baseline). b) Airfoil with tubercle leading-edge.

$$\vec{v}_f(\omega) = \int_{-\infty}^{\infty} \vec{u}_f(\tau) e^{-i\omega\tau} d\tau \tag{5}$$

Here ω is the angular frequency of the flow. The ratio of the amplitude of particle and fluid velocities can be written as follows using the Stokes drag model.

$$\frac{|\vec{u}_p|^2}{|\vec{u}_f|^2} = \frac{v_p v_p^*}{v_f v_f^*} = \frac{(18/s)^2}{(18/s)^2 + (Sk^2)^{-2}} \tag{6}$$

where $*$ represents the complex conjugate and Sk is the Stokes number defined by

$$Sk = \left(\frac{\omega}{\nu}\right)^{1/2} d_p \tag{7}$$

and s is the density ratio ρ_p/ρ_f. The Stokes number for the primary flow was found to be 0.006 and for the secondary flow was found to be 0.018. Thus, it can be said that the seed particles respond to the flow oscillations accurately for the given flow conditions.

A high-resolution feature as described in Lourenco & Krothapalli [10] is implemented in the PIV processing algorithm to obtain the velocity vectors from the particle pairs with high spatial resolution. In this algorithm, a high-resolution mode is adopted to account for the high velocity and seeding gradients that are encountered in the stall region of the flow. In this mode, the average displacement of the ensemble of particles in the interrogation area is measured using statistical correlation techniques. Thereafter, the interrogation area is further subdivided in order to identify individual particles using a particle detection scheme. A mask is applied to eliminate the effect of particle image truncation at the edges of the interrogation region and also to eliminate spurious background due to reflections and parasite illumination. The particle detection scheme

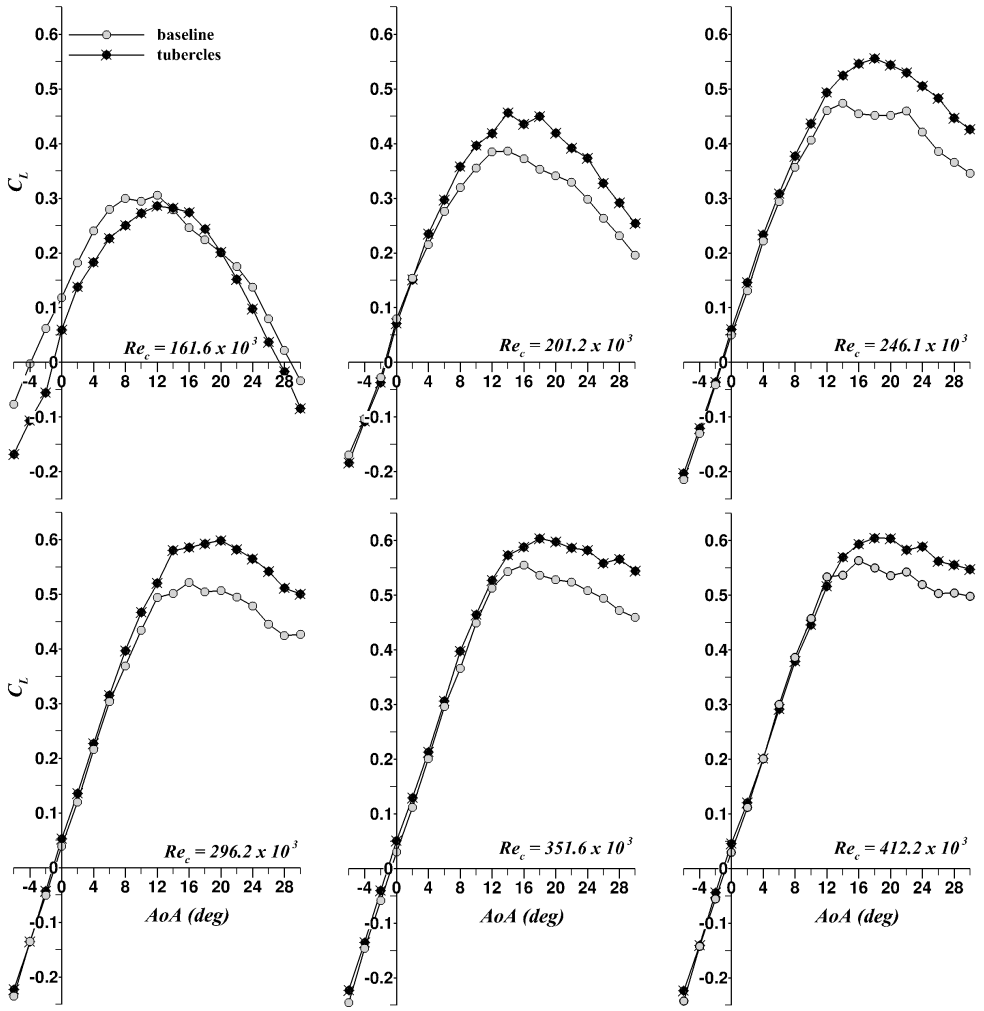

Figure 4. Variation of lift coefficient with angle of attack.

also generates a list of the center of mass, position and form factor of each particle image. Once the particles are identified, a particle pairing procedure is applied based on the group displacement. The displacement is measured based on the maximum correlation between images of corresponding particles. In this procedure, sub-pixel resolution is obtained by means of Gaussian interpolation. The measured displacement is assigned at the midpoint of the center of masses of the corresponding particle images. Using a least squares fitting algorithm, the error in each displacement measurement is minimized. Second order accuracy is maintained by assuming that the displacement field is well represented locally by a second order polynomial. The main purpose of the least squares method is to account for the velocity and seeding density gradients in addition

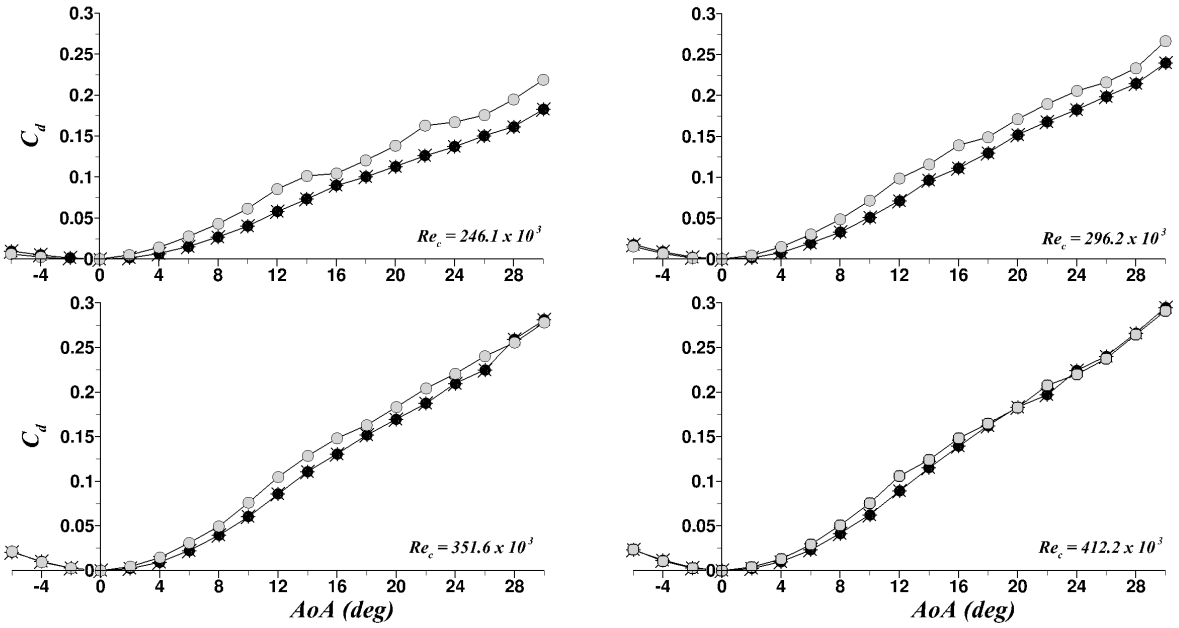

Figure 5. Variation of drag coefficient with angle of attack. Circles - baseline airfoil; Star - tubercle leading-edge airfoil.

to minimizing the local measurement error in comparison to that associated with individual particle image pairs. Even though an unstructured grid is used for obtaining the velocity vectors, the velocity field in the present study is presented at regular interval for ease of presentation. It was demonstrated by Lourenco & Krothapalli [10] that this approach improved the accuracy and the spatial resolution substantially over the traditional PIV methods. It was shown from their study that the errors were confined to the ± 0.025 pixel interval for even a large imposed displacement of 9 pixels.

D. Airfoil Characteristics

Two types of airfoils with NACA 0010 cross-section were used in this study: one with leading-edge modifications (figure 3) and one without. The span of each airfoil is 0.3048m with a chord length of 0.1524m. Leading-edge modifications in the form of tubercles were introduced as shown in the figure. The amplitude of tubercles is 6% of the chord length with 8 tubercle over the 6-inch span. The aerodynamic characteristics that are investigated include lift, drag and pitching moment for angle of attack varying from -6^0 to 30^0. Flow field characteristics such as velocity field and other derived quantities were obtained using stereo PIV measurements.

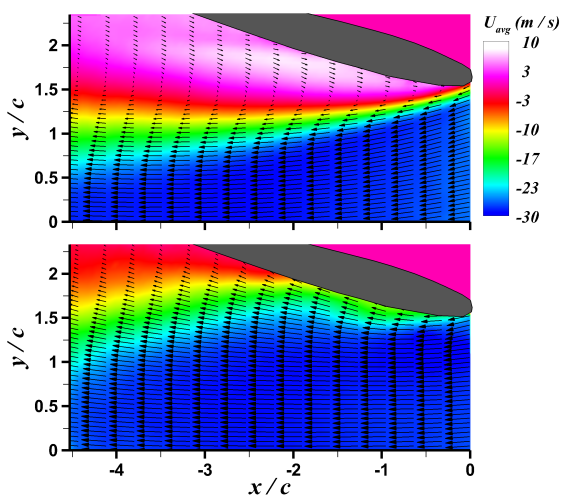

Figure 6. Mean axial velocity contours at $Re_c = 296.2 \times 10^3$, 18^0 angle of attack. Top - baseline; bottom - tubercle airfoil.

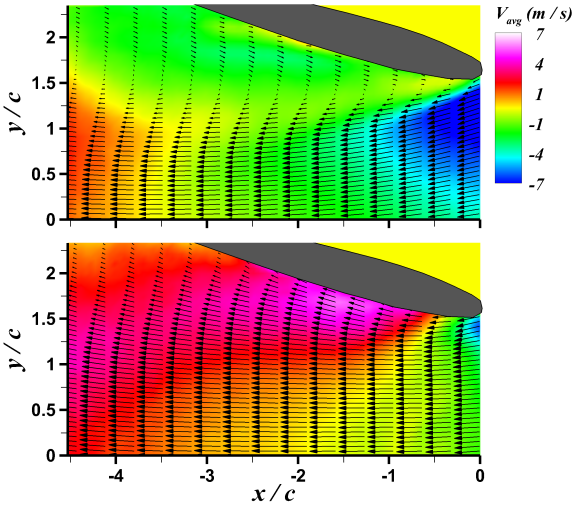

Figure 7. Mean transverse velocity contours at $Re_c = 296.2 \times 10^3$, 18^0 angle of attack. Top - baseline; bottom - tubercle airfoil.

III. Results and Discussion

A. Aerodynamic Characteristics

Figure 4 shows the variation of lift coefficient with the airfoil angle of attack over a range of Reynolds numbers based on chord length from 161,000 to 412,000. The lift coefficients were calculated from the measured lift obtained from the ATI force tranducers. The lift coefficient is defined as

$$C_L = \frac{L}{(1/2)\rho A V^2} \tag{8}$$

where L is the lift force given by $L = (F_{Ay} + F_{By})cos(\theta)$. F_{Ay} and F_{By} are the measured forces in the x and y directions of the two transducers A and B, and θ being the angle of attack. The airfoil planform area is A, ρ is the density of air and V is the freestream velocity.

At the chord Reynolds number of 161,000, it can be seen that there is performance enhancement pre-stall. On the contrary, there is a deterioration of the lift coefficient due to the presence of leading edge tubercles. For Reynolds numbers greater than 200,000, the results show that there is lift enhancement of nearly 15% both at stall and during post-stall conditions but remains nearly unchanged during the pre-stall regime. Furthermore, at these Reynolds numbers, stall is delayed up to nearly 18^o angle of attack for the

tubercle leading edge airfoil as compared with the baseline airfoil. It is also observed that during post-stall, the reduction in lift is much more gradual for the tubercle leading-edge airfoil as the Reynolds number approaches 400,000.

Figure 5 shows the coefficient of drag as a function of angle of attack for the two airfoils. The drag coefficient C_D is calculated using the following equation.

$$C_D = \frac{D}{(1/2)\rho A V^2} \tag{9}$$

In the above expression, D is the form drag measured by the force transducers. The total drag (not shown here) was also calculated by integrating the measured wake velocity profiles. The wake profiles were measured using the pitot rake at a downstream distance of $0.2c$, where c is the chord length of the airfoil. The drag coefficient shown in figure 5 indicates that while there is an apparent reduction at $Re_c = 246.1 \times 10^3$ for the tubercle leading-edge airfoil as compared to the baseline airfoil, at higher Reynolds numbers tested, the drag reduction due to tubercles, while still present, is considerably smaller. It is also seen from the data that as the angle of attack is increased in the post-stall regime, the drag reduction benefit begins to disappear at angles of attack greater than 24^0.

Figure 6 shows the comparision of mean axial velocity contours for the baseline airfoil and the tubercle leading-edge airfoil at $Re_c = 296.2 \times 10^3$ and 18^0 angle of attack. This angle of attack falls in the post-stall region for both airfoil configurations. The mean velocity was calculated by taking the average of 1500 instantaneous velocity fields. The results show that for the baseline configuration, flow separation takes place almost immediately at the leading edge. However, for the tubercle-leading-edge configuration, separation is delayed to a downstream location of about $x/c = 2$. The data also shows a large recirculation region following flow separation for the baseline airfoil. Significant difference, however, can be noticed for the tubercle leading-edge airfoil configuration with the recirculation region being completely absent. An examination of the transverse velocity contours (figure 7) showing positive transverse velocities at all downstream locations on the tubercle leading-edge airfoil as opposed to mostly negative transverse velocities for the baseline configuration also confirm the absence of recirculation region for the tubercle configuration. The delayed separation and absence of recirculation region in the tubercle leading-edge configuration can be

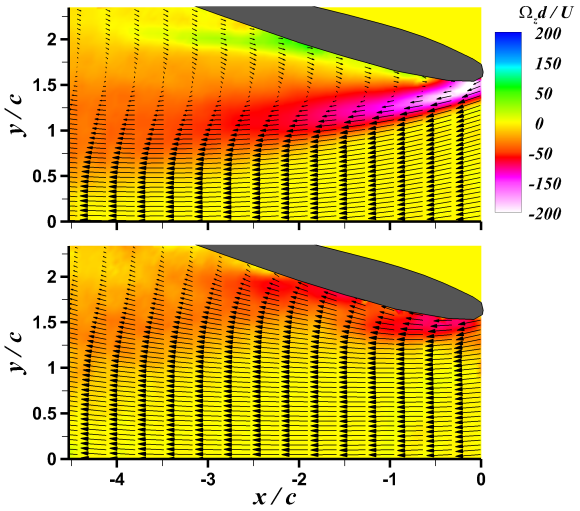

Figure 8. Mean vorticity contours at $Re_c = 296.2\times10^3$, 18^0 angle of attack. Top - baseline; bottom - tubercle airfoil.

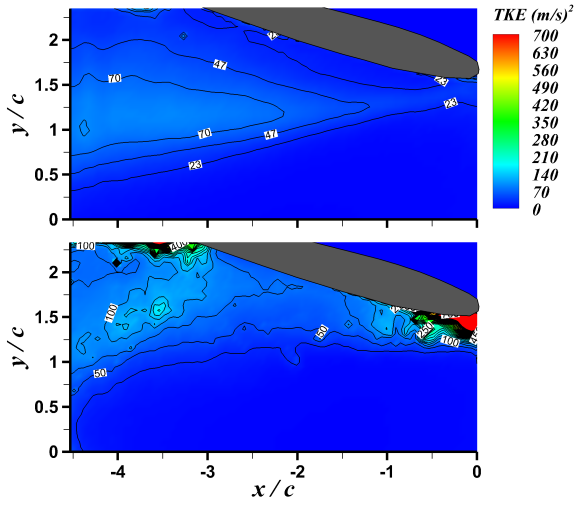

Figure 9. Mean turbulent kinetic energy at $Re_c = 296.2\times10^3$, 18^0 angle of attack. Top - baseline; bottom - tubercle airfoil.

explained from the mean vorticity contours (figure 8 and the mean turbulent kinetic energy (TKE) contours (figure 9). The vorticity contours for the tubercle leading-edge airfoil show concentrated vorticy on the surface of the airfoil up to a downstream distance of about $x/c = 2$. The presence of vorticity on the surface of the airfoil is due to the increased momentum exchange within the boundary layer due to streamwise vortices generated at the peaks and troughs of the tubercle leading-edge. An indication of this phenomena can be seen in the TKE contours. The TKE contours show a large amount of turbulent mixing at the leading edge of the tubercle airfoil configuration. The increased momentum exchange and flow mixing leads to delayed stall and a larger lift coeffcient for the tubercle leading-edge configuration.

IV. Conclusions

The aerodynamic and flow field characteristics of a NACA 0010 airfoil with and without leading-edge tubercles were investigated over a range of Reynolds numbers from 160,000 to 412,000 with a freestream turbulence intensity of 4%. The results showed that the tubercle-leading-edge airfoil achieved little to marginal performance enhancement pre-stall. However, at stall and in the post-stall region, substantial performance enhancement was observed within the range of Reynolds numbers tested. The flow field data obtained using PIV showed large amount of turbulent mixing at the leading edge of the tubercle airfoil configuration, in

part augmented due to the high freestream turbulence intensity, thus delaying flow separation, and hence leading to delayed stall and a higher lift coeffcient as compared to the baseline airfoil configuration.

References

[1]Ott, R.L., "An Introduction To Statistical Methods and Data Analysis", Duxbury Press, Belmont, California ,1993.

[2]Rohsenow, W. M., Choi, H., "Heat,Mass and Momentum Transfer", Prentice-Hall Inc., New Jersey, 1961, pp. 192-193.

[3]Hinze, J. D., "Turbulence, An Introduction to its Mechanism and Theory", McGraw Hill, 1959.

[4]Alkislar, M. B., Krothapalli, A., and Lourenco, L. M., "Structure of a screeching rectangular jet: a stereoscopic PIV Study," *Journal of Fluids Mechanics*, Vol. 489, 2003, pp. 121–154.

[5]Choutapalli, I. M., "An Experimental Study of a Pulsed Jet Ejector," PhD Dissertation, Florida State University, 2006.

[6]Ross, C. B., "Calibration of particle image velocimetry in a shock-containing supersonic flow", M.S. thesis, Florida State University, Tallahassee, 1993.

[7]Mei, R., "Velocity fidelity of flow tracer particles," *Experiments in Fluids*, vol.22, pp. 1 13, 1996.

[8]Hjelmfelt, A. T. and Mockros, L. F., "Motion of discrete particles in a turbulent fluid", Appl. Sci. Res., Vol. 16, No. 1, pp. 149-161.

[9]Prestridge, K., Rightley, P., Vorobieff, P. and Benjamin, R., "Simultaneous density-field visualization and PIV of a shock-accelerated gas curtain", Exp. Fluids, Vol. 29, No. 4, pp. 339-346, 2000.

[10]Lourenco, L. M. and Krothapalli, A., "True resolution PIV: A mesh-free second-order accurate algorithm", *Proceedings of the 10th International Symposium on Applications of Laser Techniques in Fluid Mechanics*, Lisbon, Portugal, 2000.

[11]Gad-El-Hak, M., "Flow Control", Cambridge University Press, 2000.

[12]Earl M. Uram, "Laminar turbulent boundary layers", *presented at American Society of Mechanical Engineers Energy Sources Technology Conference*, New Orleans, Louisiana, February 12-16, 1984.

[13]F. Noca, D. Shiels and D. Jeon, "A comparison of methods for evaluating time-dependent fluid dynamic forces on bodies, using only velocity fields and their derivatives", *Journal of Fluids and Structures*, Vol. 13, Issue 5, pp. 551-578, July 1999.

[14]Jie-Zhi Wu, Hui-Yang Ma and Ming-De Zhou, "Vorticity and vortex dynamics", Springer Press, 2005.

[15]Bechert, D. W., Bruse, M., Hage, W., Hoeven, J. G. T. V. D., and Hoppe, G., "Experiments on Drag-Reducing Surfaces and Their Optimization with an Adjustable Geometry", J. Fluid Mech., Vol. 338, pp. 59-87, 1997.

[16]Bushnell, D. M. and Moore, K. J., "Drag reduction in nature", Ann. Rev. Fluid Mech. 23:65-79, 1991.

[17]Fish, F. E. and Battle, J. M., "Hydrodynamic design of the humpback whale flipper", J. Morph 225:51-60, 1995.

[18]Bearman, P. W. and Owens, J. C., "Reduction of bluff-body drag and suppression of vortex shedding by the introduction of wavy separation lines", J. Fluid Struct. 12:123-30., 1998.

[19]Johari, H., Henoch, C., Custodio, D. and Levshin, A., "Effects of leading-edge protuberances on airfoil performance", AIAA J., 45:2634-42, 2007.

[20]F. E. Fish "Performance constraints on the maneuvaribility of flexible and rigid biological systems", *Proceedings of the 11th International Symposium on Unmanned Untethered Submersible Technology*, Autonomous Undersea Institute, Durham, NH, 1999.

II. List of Personnel Supported

The following is the list of personnel supported during the course of the AFOSR grant (2014 – 2018).

Faculty:
---

1. Dr. Isaac Choutapalli – PI: Supported for three summer months

Graduate Students:
---

1. Mr. David Cano, MS student (graduated): Supported for two years
2. Mr. Greg Acosta, MS student (graduated): Supported for two years, partly by mechanical engineering department as well.
3. Mr. Oscar Hernandez, MS student (graduated): Supported for two years, partly by mechanical engineering department as well.

Undergraduate Students:
---

1. Ms. Alexandra Alaniz, UG student (graduated): Supported for two years
2. Mr. William Rektorik, UG student (graduated): Supported for two years
3. Mr. Josue Botello, UG student (graduated): Supported for one year
4. Ms. Roxana Molina, UG student (graduated): Supported for one year, partly by mechanical engineering department.
5. Mr. Jean Calzada, UG student (graduated): Supported for one year, partly by mechanical engineering department.

III. List of Publications

The following is the list of publications based on the work done during 2014 - 2018.

Conference Proceedings:
---

1. A. Martinez-Ibarra, G. Acosta, R. Freeman and I. Choutapalli, “Characteristics of Leading-Edge Tubercle Airfoil in Flow with High Freestream Turbulence", AIAA SciTech 2019, San Diego, CA, January 7-11, 2019, AIAA 2019-1104.
2. A. Martinez-Ibarra, R. Freeman and I. Choutapalli, “Aerodynamic Characteristics of Bio-Inspired Wings with Spanwise Waviness in a Turbulent Freestream", 72nd Annual Meeting of the APS Division of Fluid Dynamics, DFD19-2019-002248, Seattle, WA, November 23-26, 2019.

Journal Articles:
---

1. A. Martinez-Ibarra, G. Acosta, R. Freeman and I. Choutapalli, “Effect of Freestream on Aerodynamic Performance of Wings With Leading-Edge Modifications", In preparation for submission to the *Journal of Aircraft*.

IV. Outreach Activities

The University of Texas – Rio Grande Valley is a minority institution (Hispanic Serving Institution) serving mostly Hispanic students located in Edinburg, Texas in the Rio Grande Valley (Hidalgo County) in south Texas. The university has more than 85% of students who are of Hispanic origin. The unique opportunity has provided the ideal conditions to reach out to the underrepresented minority students and provide them the opportunity to participate in cutting-edge flow control research in the PI's laboratory. ***During the course of the work (2014 – 2018), the research work supported by AFOSR was showcased to approximately 300 high school and middle school students in the Edinburg McAllen-Pharr area of south Texas***. This outreach program is called Hispanic Science and Engineering (HESTEC). Hispanic, Engineering, Science, and Technology (HESTEC) Week is organized by the University of Texas-Pan American, one of the country's top Hispanic serving institutions. Since its inception, HESTEC has become a national model for promoting science, technology, engineering and math careers among South Texas students who are predominantly Hispanic. HESTEC is a year-round program that culminates in a weeklong event held on the UTPA campus. During this week, events are held for educators, students and parents that promote science literacy. ***HESTEC has provided an ideal opportunity for the PI to showcase the cutting-edge research in flow control and reach out and identify student talent, encourage them to pursue higher education and recruit them to participate in the PI's research***.

V: APPENDIX-A LITERATURE REVIEW

Background

Aircraft Drag Reduction

Finding new ways of reducing drag on aerodynamic bodies has been of interest since the earlier 1970's due to the fuel crisis and now in our on current age, where fuel prices are considerably high; these ideas of reducing drag are still of much prime importance, especially to military and civilian aircraft. By simply reducing a ten percent of drag on a C-5 transport aircraft, it could have the potential to save millions of dollars in fuel.

There are many contributors of drag; for example, skin-friction drag which is due to the viscosity of the air, lift-induced drag due to the conserved circulation developed around the wings. Pressure drag due the open separation in the after body and other regions, interference effects between aerodynamic components, wave drag due to compressibility effects at near-sonic flight conditions and miscellaneous effects such as roughness effects and leakages. All these types of drag add up to form what is called the total drag of the aerodynamic body. Figure 1.1 depicts how each individual type of drag contributes to the total drag, notice how much of the induced and skin-friction drag contribute to the overall drag.

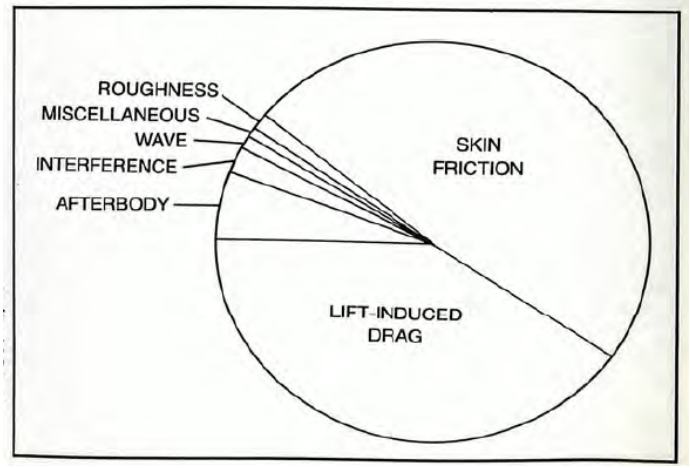

Figure 1: Diagram depicting the contribution of each element to the total drag

This implies that most of the drag is generated by the friction of the air, where a thin boundary layer is forming on the surface of the wing, and secondly by induced drag at the tips of the wings due to the cross flow or the three-dimensional effects of a wing. The main reason why the skin-friction drag is dominant on the total drag is due to the fact that most of the airflow is attached to the wing when at steady level flight; thus, hindering a friction due to the viscosity and tangential forces on the surface of the wing. However, when an aircraft goes under stall the effects of pressure drag dominate over all other types of drag, due to the flow separating on the body as discussed previously, in this case flow separation on a wing. Knowing the region where an aircraft stalls is important because it determines the maximum lift and hence the maximum lift coefficient generated by a wing, it also determines the stalling velocity or the lowest possible velocity, which an aircraft can maintain steady level flight. As result of the effort to reduce drag on an aircraft, various technologies have been developed over the time; for example, to reduce skin-friction drag, suction ports are implemented on the surface of the wing to maintain laminar flow, another concept consists of using riblets on the surface which provide momentum exchange between the flow. To treat induced drag, winglets are utilized at the tip of the wings. Winglets reduce drag by creating a

thrust component due to the lift force on the winglet itself, measuring the thrust component would be obtaining a measurement of how much induced drag is reduced at the wing tips.

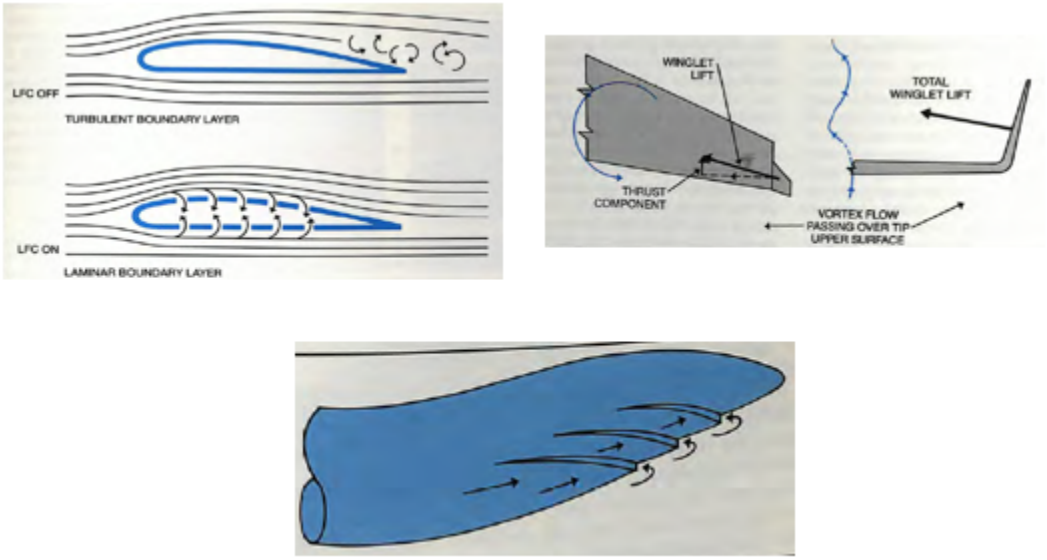

Figure 2: Various aircraft reduction technologies

Drag Reduction in Nature

One source of inspiration for alternative drag reduction approaches is the study of Avions and Nektons, in order words fliers and swimmers; the presumption has been that these creatures have developed various way to reduce drag in a natural way, which provides better efficiency and speed. This leads to the study of the humpback whale (*Megaptera novaeangliae*) and the question of how can this swimming creature of tremendous size, maneuver so efficiently while catching its prey. Researchers observed the pectoral fin of the whale and its characteristics of reducing drag due to lift. These fins have a special geometry that enables them to maintain lift while at high angles of attacks and thus allowing them to perform complex rotating maneuvering loops. The pectoral fin consists of tubercles or protuberances located at the leading edge of the fin.

Figure 3: Humpback whale showing tubercles on the pectoral flipper.

Compared to vortex generators or passive-flow regulating structures, the tubercles prolong the attachment of the flow field on the surface of the wing. They provide momentum exchange between the boundary layer, analogous to the riblets mentioned previously; therefore, this will result in a delayed stall. It's known that the tubercles produce a pair of stream wise counter rotating vortices, but the way in which these vortices interact with flow over a foil or wing is still unknown. Even though the phenomena is still unclear, researchers have proposed theories, but some standout, which they are widely accepted. The first is that the tubercles act as vortex generators as mention before and the second where downwash occurs, it's suggested that the effective angle of attack is reduced, resulting in an increase stall angle, whereas the opposite will occur where there is up wash. Another proposed theory suggests that the stream wise counter rotating vortices created by the tubercles could manipulate the flow in a similar fashion as the delta wing. Form these theories, it can be said that not only one mechanism is present, but a combination of such mechanisms. Research conducted on the tubercles have found that not only does the bumps delay stall but also

reduces drag and increases lift, thus making the wing more efficient; findings made on the tubercles will be discussed later.

Aerodynamic Parameters

First, it is important to define some important aerodynamic parameters that will help characterize the lift and drag on an airfoil and wing:

$$q_\infty = \frac{1}{2}\rho_\infty V_\infty^2 \tag{1.1}$$

$$C_l = \frac{L'}{q_\infty c} \tag{1.2}$$

$$C_d = \frac{D'}{q_\infty c} \tag{1.3}$$

$$C_m = \frac{M'}{q_\infty c^2} \tag{1.4}$$

$$\frac{L}{D} = lift\ to\ drag\ ratio \tag{1.5}$$

$$R_e = \frac{\rho V_\infty c}{\mu} \tag{1.6}$$

Equation 1.1 is simply the dynamic pressure of the free stream conditions; notice the superscript on the lift, drag and moment of equations 1.2-1.4; these denotes a two-dimensional airfoil where for example *L*' describes lift force per unit span and consequently the lift, drag and moment coefficients are written with lower case letters. If considering a wing, then the coefficients are written in uppercase letters. Equation 1.5 is a measure of the aerodynamic efficiency of an airfoil or wing; in other words, how much is the wing being penalized with drag, for lift generated. Equation (1.6) is simply the Reynolds number for a characteristic length, in this case the chord length. Reynolds number is very important parameter when considering experimentation of

aerodynamic bodies. It can describe the flow conditions, for example if the flow is laminar, or turbulent. Another important aspect of the Reynolds number is establishment of flow similarity between two bodies of different size scale. In other words, if the one wants to test a prototype of an airplane inside a wind tunnel, the Reynolds number must equal. By establishing flow similarity, one can safely transfer their results to actual flight conditions. As for the main difference between a two-dimensional airfoil and a three-dimensional wing is the presence of cross-flow for the wing; a 2D airfoil neglects the effects of cross-flow and thus the wing tip vortices generated by such flow. In experimentation, spanning the airfoil entirely across the test section will accomplish such conditions, for example inside a sub-sonic wind tunnel.

Contrast from Inviscid to Viscid Fluid Flow

Ideal fluid flow or inviscid, low speed fluid flow refers that the ideal case where a fluid's viscous and compressibility's effects due to the density can be neglected. These assumptions facilitate the aerodynamicist in obtaining an analytical solution for the fluid flow around a body or in other words the pressure distribution on the surface. Neglecting the compressibility effects requires for the flow to engage in speeds of less than 30% of the speed of sound or Mach 0.3; this can be achieved in experimentation by maintaining the speed of the flow at this requirement

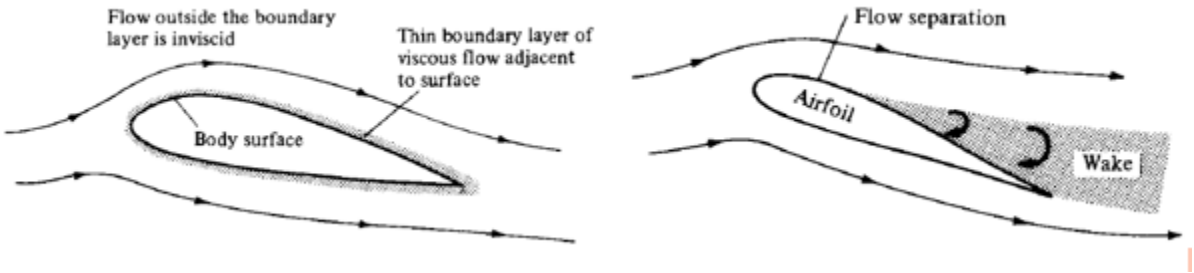

Figure 4: Airfoil before and after flow separation

Inviscid refers to the case where the fluid's viscous effects can be neglected, but in nature no flow is inviscid. For example, when an airfoil undergoes a pre-stall condition or in other words the flow

is completely attached to the surface; a thin boundary layer is formed on the surface due to the viscous effects of the air. This boundary layer inflicts shear or tangential forces on the surface and thus forming skin friction drag. One of the reasons why most of the total drag is compose of skin friction on an aircraft is due to flow attachment to the surface at steady level flight. As stated before assuming inviscid flow facilitates obtaining an analytical solution to flow around a body and to a certain degree it can be accurate but it cannot predict or tell anything about the surface of the body since the thin boundary layer formed is attributed exclusively to the viscous effects of the fluid flow. After an airfoil stalls it enters the post-stall regime and most of the flow is dominated by the viscous effects; because of the flow separation throughout the whole flow field. The highly separated flow forms a larger boundary layer.

Literature Review

One of the first papers published with results for the humpback whale pectoral fin, was that of D.S. Miklosovic et al. They tested a set of polycarbonate scale models of the whale's flipper with and without leading-edge tubercles. The flipper planform geometry was modeled, roughly after a left pectoral flipper of 9.02m; as for the flipper cross sectional profile, a symmetrical NACA 0020 airfoil section was chosen, due to the fact, the flipper cross sectional profile is similar to conventional turbulent flow airfoils with maximum thickness of approximately 20%. The machined models done on a CNC mill; achieved a maximal chord of 16.19 cm and a span of 56.52 cm, the following figure depicts the models:

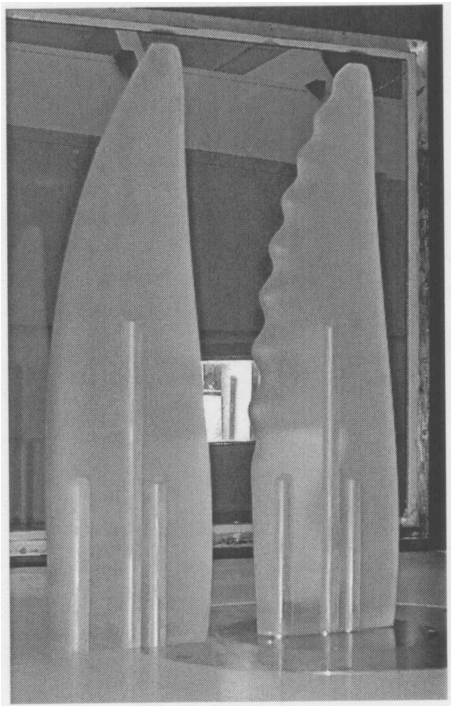

Figure 5: Model of the humpback whale pectoral fin

Conducted testing performed in a low speed closed-circuit wind tunnel located at the United States Naval Academy, met incompressible flow conditions. Wind Tunnel experiments at uncorrected Reynolds numbers in the range of $5.05 \text{ X } 10^5 – 5.20 \text{ X } 10^5$ as reference to the freestream velocity, mean chord and the kinematic viscosity of air; yield favorable results and an insight of the possible advantage of the tubercles. A six-component force balanced, measured the aerodynamic forces, for example lift and drag. In order to establish a Reynolds number sensitivity, the Reynolds number was varied from 135,000 to 550,000, the lift and drag coefficients were measured at angles of attack of 0° and 5°. Although both the lift and drag coefficients show a notable dependence at the lower Reynolds numbers, the curves flatten out to indicate very little or no Reynolds number dependence at the test conditions of the present study. They found out that the lift coefficient is the most insensitive, with essentially no dependence for the Reynolds number above 200,000, which is key since our present research will operate above that range. The following figure show the results obtained for the both smooth and modified leading edge:

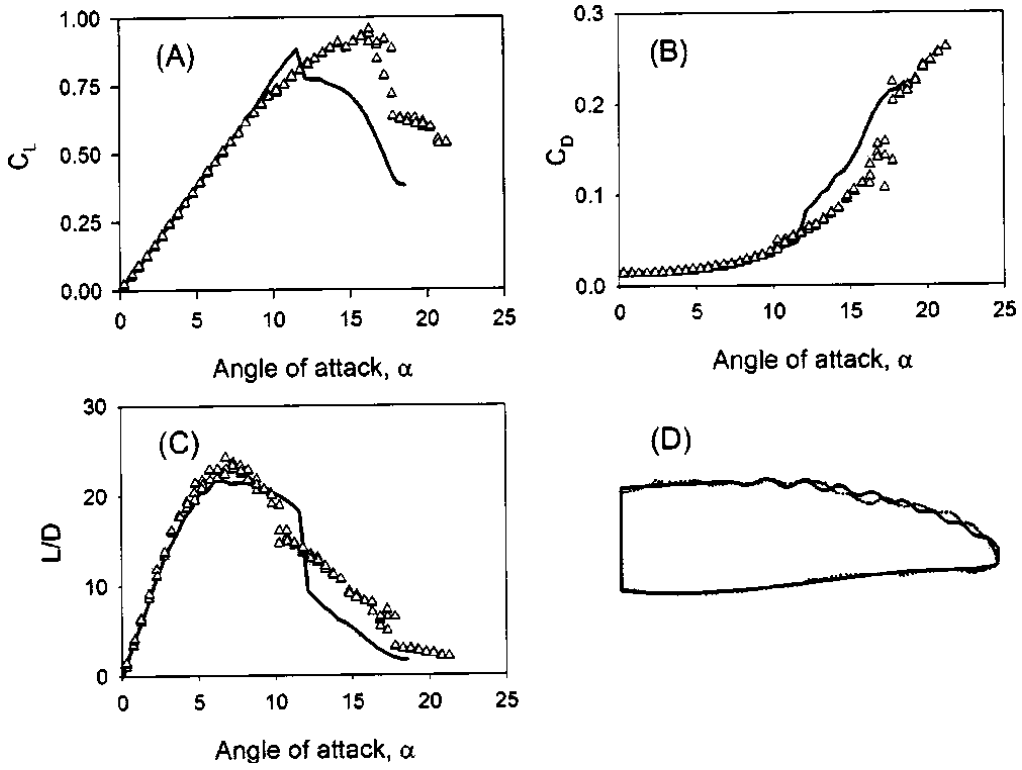

Figure 6: Results obtained for Miklosovic et al.

In figure 1.4, plotted are the lift coefficient, drag coefficient and lift-to-drag ratio vs. angle of attack, the solid line depicts the smooth flipper, while the dotted line depicts the modified flipper with tubercles. Clearly, from the figure, the aerodynamic properties improved especially after a stall angle of approximately 12° for the smooth flipper. The maximum lift coefficient increase to almost of an angle of 16° and thus an indication of an increase of lift; the drag coefficient was also improved; hence, an improvement in aerodynamic efficiency for higher angles of attack. Most of the aerodynamic properties were unchanged during pre-stall except for drag, which showed a small improvement during, but the contrary happened for post-stall, where all the properties improved. Miklosovic et al. concluded that the tubercles acted as vortex generators delivering momentum exchange between the boundary layer. This additional momentum transport helps to keep the flow attached to the lifting surface despite an adverse pressure gradient.

Another study conducted by H. Johari et al, investigated the aerodynamic loading resulting from the presence of leading-edge protuberances on a NACA 63_4-021 having a range of protuberance amplitudes and spanwise wavelengths. The chose for the cross section profile was that of a six series NACA airfoil because it resemble that of the humpback whale, as shown in figure 1.5.

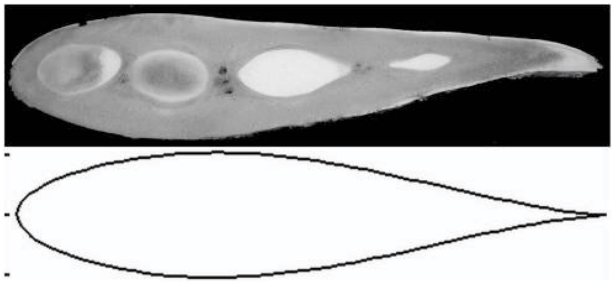

Figure 7: Comparison of a humpback whale pectoral flipper cross section with NACA 6 series

The focus behind this investigation was the study of steady flow over two-dimensional airfoils, which previous conducted studies were only for finite wings. Performed experimentation inside a water tunnel; allowed achieving flow visualization on the surface of the airfoil. A fiber optic laser Doppler velocimetry (LDV) system monitored the free stream velocity and a load cell captured the aerodynamic forces. The following figure shows the results obtained by H. Johari et al; all the data reported was taken at freestream velocity of 1.8 m/s, which yielded a Reynolds number of 183,000:

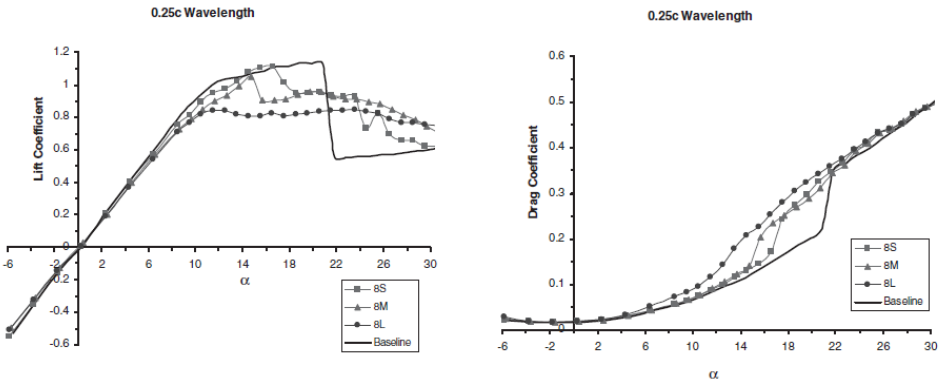

Figure 8: Results obtained by H. Johari et al.

Figure 1.6 shows the lift and drag coefficient as a function of angle of attack, for a wavelength of 25% of chord length. The amplitude is represented by S, M, and L on the figure where they equal to 0.025*c*, 0.05*c* and 0.12*c* (percentage of chord length) respectively. As seen on the figure, the outcome of the results for a two-dimensional airfoil demonstrated the contrary as that of a finite wing; lift and drag coefficients were reduced when protuberances are located on the leading edge of an airfoil. Even though the coefficients were jeopardized, the steep decline of lift in the post-stall region was reduced considerably. Amplitude of the bumps demonstrated an apparent effect on how the post-stall behavior of the airfoils. Larger amplitudes tend to have a more gradual delay of stall and keeps the lift coefficient constant for a prolonging angle of attack. As for the smaller amplitude, it demonstrated the best aerodynamic properties with a higher lift coefficient. The drag coefficient demonstrated no benefits from the protuberances on the leading edge. Flow visualization using surface tufts revealed that the flow over the protuberances remained attached well past the angle of attack here the baseline airfoil stalls. When flow separation occurs, it was observed that in mainly occur in troughs between the bumps. It was concluded that wavelength have a minor effect on the flow characteristics, it has been suggested that there is an optimal configuration of amplitude-to-wavelength ratio. A suggestion for the phenomena is not given; however, H. Johari et al. also tested two different configurations of the leading-edge bumps, where it was found that there was no or little effect on the results of the airfoils.

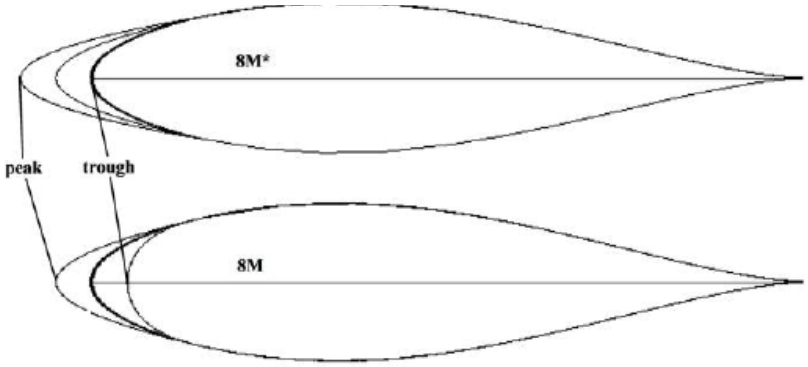

Figure 9: Different configurations for the leading-edge bumps

So far, all the present work has involved exclusively experimentation work, but a good insight on the effect of tubercles on a leading edge of a wing can be done by establishing an aerodynamic model. A model was proposed by E. van Nierop et al; this model is the basis for our aerodynamic model. To understand the role of the bumpy tubercles, a simple model of a smooth wing was considered. It showed how the aerodynamic properties of the wing were affected by the bumps on the leading edge. The model also considers a chord length that varies on a length scale compared with its thickness. By taking a Joukowski profile, van Nierop et al. was able to establish an expression for the circulation around the wing (1.7) and as for representing the bumps on the leading, a series perturbation was used (1.8).

$$\Gamma = -\pi U_0 (c + \frac{4}{3\sqrt{3}} t)\alpha^e + O((\alpha^e)^3, t^3) \tag{1.7}$$

$$S = \frac{1}{c_0} \sum_{k=1}^{\infty} a_k \cos(k\theta) \tag{1.8}$$

Equation 1.7 implies that the variation of the chord and thickness along the wing causes a variation in the circulation Γ. Such span wise changes in the circulation generate a sheet of stream wise vortices behind the wing, which causes the effective angle of attack to vary along the wing. By

simply using the lifting-line theory, which allows representing a wing as a single vortex line of varying strength along the span, calculating the magnitude of the downwash is as follows:

$$w = \frac{1}{4\pi}\int_{-s}^{s}\frac{d\Gamma / dy'}{y - y'}dy' \tag{1.9}$$

And the lift force can be calculated by,

$$L = \rho U_{\infty}\int_{-s}^{s}\Gamma(y)\,dy \tag{1.10}$$

In order to solve for the integral equation and thus the circulation, a Chebyshev series was utilized to expand the effective angle of attack and consequently the circulation in orders of thickness/chord ratio and bump amplitude. This expansion allowed to represent the circulation as series perturbation and reproduced the result that lift is proportional to the angle of attack for an elliptic wing. The results for the aerodynamic model are shown in the following figure; which were compared to H. Johari et al.

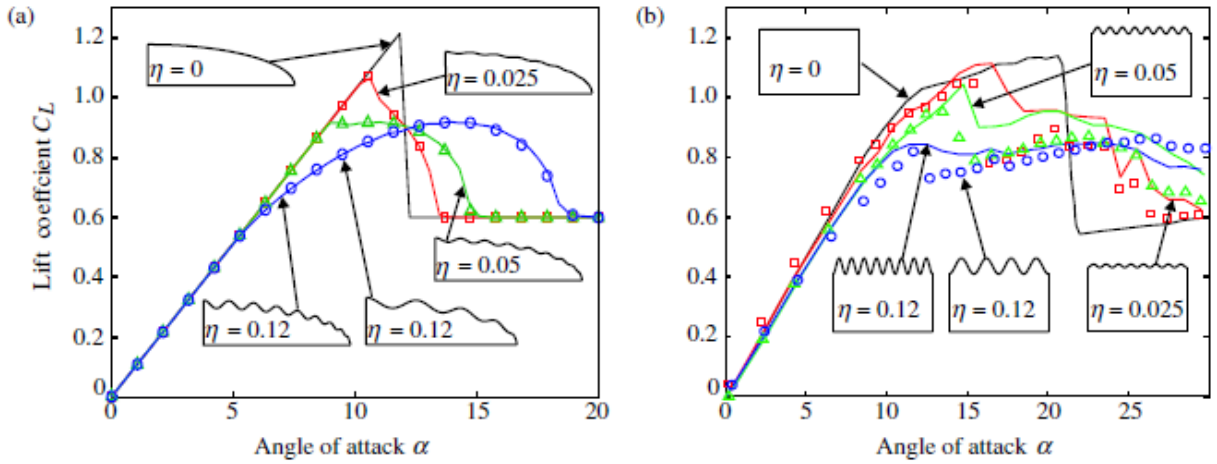

Figure 10: (a) Results for aerodynamic model established by van Nierop et al (b) Results from Johari et al.

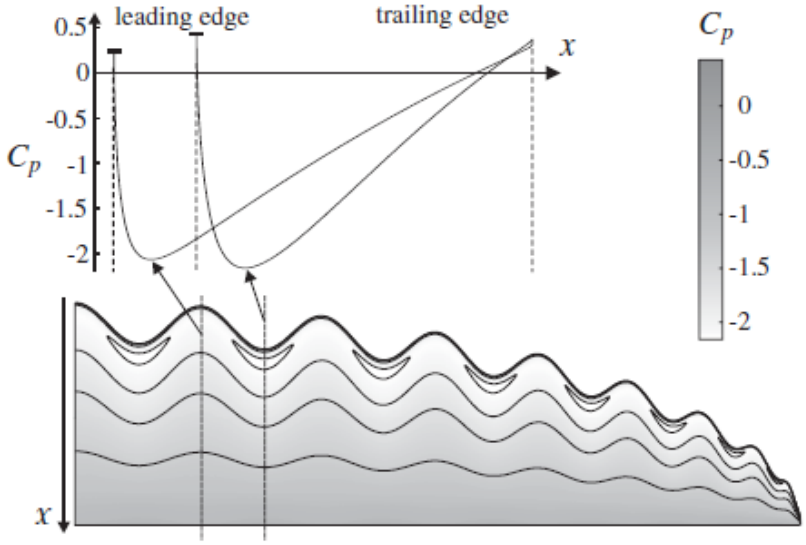

Figure 11: Calculated pressure distribution on the bump and trough

In addition to predicting delayed stall, calculations agree with many other aspects of the experiments. In conclusion, note that the results on Figure 1.7 captures the main features exhibited by wing section or airfoil experiments, notably, a more gradual stall and a higher overall stall angle. The original experiments by Miklosovic et al. showed a larger maximum lift coefficient and somewhat sudden stall. The present model nor H. Johari et al. and other experiments on airfoils reproduce these features. This may because airfoils do not account for the wing tip effects and the aerodynamic model cannot accurately predict at the tips due to singularities.

VI: APPENDIX-B EXPERIMENTAL SET UP

AERODYNAMICS LABORATORY

Facility Equipment

Open Circuit Wind Tunnel

The University Of Texas Rio Grande Valley is equipped with an open circuit wind tunnel that draws airflow directly from the atmosphere at the inlet through the tunnel circuit. Powered by a 60 HP electric motor, the wind tunnel can reach speeds of approximately 45 m/s (100 MPH) and Mach numbers of 0.10 inside the test section; these are an indication that the compressibility effects can be neglected since the Mach number falls less than 0.30. The wind tunnel has a contraction ratio of 7.3; a test section consisting of a 24'' by 24'' cross-sectional area; with high visibility to facilitate the use of laser diagnostics, for example Particle Image Velocimetry (PIV). All the previous Plexiglas was replaced to with new acrylic Plexiglas. The reason behind was because the previous Plexiglas was in poor condition in terms of visibility; this can jeopardize the outcome of the laser diagnostics and thus data taken from experiments. The floor of the test section was modified to accommodate for a clear section to shoot the PIV laser from. The slot was cut out by an in-house plasma CNC cutter and once installed back in the test section, the slot was replace with new section of acrylic Plexiglas. In addition, an extra layer of Plexiglas was installed in between the outside Plexiglas (sealing the test section) and both upper and lower surfaces of the test section. The reasoning behind this was the fact that the walls perpendicular to

both upper and lower surface were not completely flush with a smooth transition and created a gap in between the walls. Therefore, the uniformness of the incoming flow can be disturbed with the presence of turbulent flow or in other words the motion of a fluid having local pressures and velocities that fluctuate randomly and thus again contaminate the gathered data with noise or with an increase of the turbulence intensity (TI). The TI is an index used to determine the flow quality inside the test section; when it comes to wind tunnel testing and proving the validity of the measurements obtained using aerodynamic tool it is desired to obtain a TI less than 0.57%. Our previous graduate student, David Cano was able to measure a turbulence intensity of 0.18% at a Mach number equal to 0.09 by using turbulence spheres.

Figure 12: Wind Tunnel Test Section

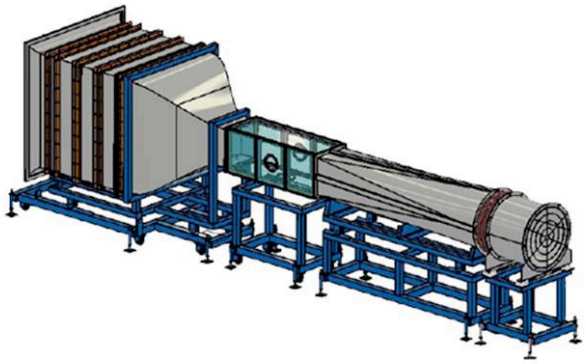

Figure 13: The University of Texas Rio Grande Valley low speed wind tunnel

Pressure Measurements

The wind tunnel was equipped with 2 OMEGA PX653-50BD5V highly accurate low pressure transducers with a range of +/- 50 inches of H2O and voltage output of 1-5 Vdc. Transducers were pre-calibrated by the manufacturer and from the calibration data sheet, one is able to obtain a calibration equation, which translates the raw voltage output to an actual pressure measurement. The transducers consist of a high and a low port for the airflow, which are connected to a pitot probe via Tygon tubing. The high port on the transducer is connected to the total pressure and the low port to the static pressure of the pitot probe respectively.

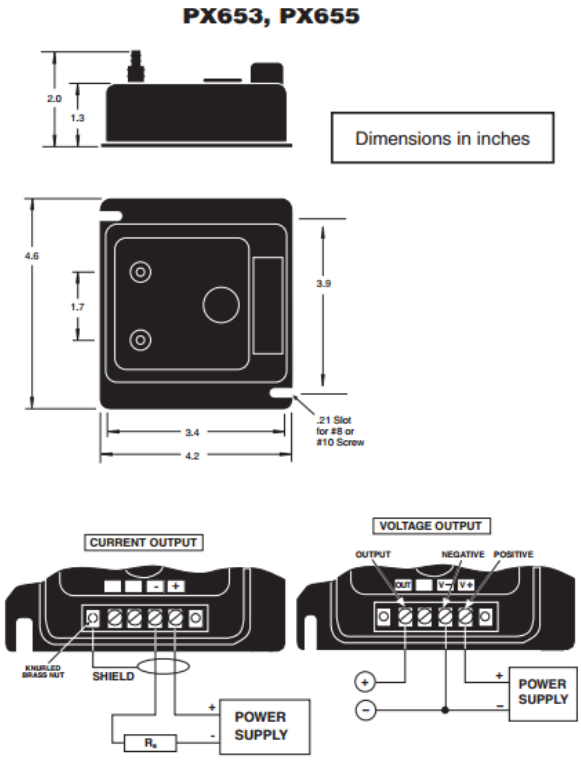

Figure 14: Omega engineering PX653 pressure transducer

A pitot probe measures the total pressure (usually atmospheric pressure) and static pressure or the random motion of the fluid particles colliding together and by using Bernoulli's principle; it is generally simple to calculate the air velocity inside the test section. These allowed for the calibration of the actual wind tunnel and it is now possible to know the actual air velocity at each different percentage in terms of the maximum frequency (Hz) or duty cycle of the electric motor.

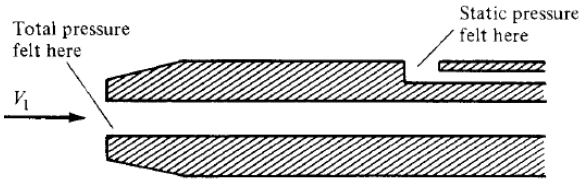

Figure 15: Schematic of pitot probe

A stepper motor was also installed to the pitot probe for automation purposes and hence a more efficient way of gathering measurements. For example, in order to measure the wake behind an

aerodynamic body inside a wind tunnel, a pitot probe is utilized to measure the velocity distribution behind the body. This requires the pitot probe to move in vertical direction at different increments. Without a stepper motor, running experiments can be more of a time consuming and therefore impact the outcome of the research. The issue with the current stepper motor is that the required stepper driver is missing, but this problem was fixed by linking a different driver (Velmex) to the motor via investigating the components of both the driver and motor. After looking up for the manufacturer's specifications, the motor, which consisted of an 8-wire motor, was connected to a 6-wire input driver and resulted in successfully controlling the stepper motor. Besides being connected to a stepper motor, the pressure transducers are also connected to process meters that display the live pressure inside the test section. Another main function of the process meters is to excite the transducers and therefore supply a voltage. A National Instruments data acquisition board was also connected to the process meters to obtain the measurements via LabVIEW, since the process meter has the capability of outputting a voltage. For all these, the process meter needs to be scaled to the proper settings (depending on the specifications of the transducer) in order to display the correct data and set for appropriate excitation parameters for the transducers.

Pressure scanner

To calculate the aerodynamic forces, a pressure scanner will be utilized to obtain the pressure distribution on the surface of the airfoils. Since, no matter how complex the geometry of the body might be the aerodynamics forces are entirely due to the pressure and shear distributions on the surface of the body. Sixteen small pressure transducers with a range of 20 inches of H2O, are housed inside a pneumatic system which are joined to 16 ports, one for each transducer, and basically the ports will be connected to the airfoil's pressure tabs located on the upper surface. The pressure scanner also has the capability of running with LabVIEW.

Figure 16: Pressure scanner Model 9116

ATI Force/Torque Transducers

A nice and convenient way of measuring the lift and drag of an airfoil is to equip the airfoil with a force and torque transducer. Functionality of a force /torque sensor consists of strain gauges mounted on beam like structure, that under deformation the strain gauges will output a voltage output. This voltage output can be calibrated such that one can obtain a calibration curve and then re-run the test to obtain force measurements. The airfoil was equipped with two ATI six axis F/T transducers; six-axis meaning that the transducer can read forces in the x, y and z components and its corresponding moments about each axis respectably. The sensing the ranges of the transducer consist of 50 lbf on both x and y axis, and a 150 lbf on the z axis. As for the sensing range of the moments, it consists of 150 lbf-in in all three axes. Calibration for the transducers were made by ATI and provided. The transducers have the capabilities of data acquisition via a National Instruments PCB card. This will allow the user to control or take readings from a LabVIEW interface and conveniently save the data in corresponding files. Proper installation of the transducer is required to obtain accurate data readings. Readings from the force transducers can be compared with data obtain form other means for example pressure transducers.

Figure 17: ATI F/T Transducer

Rotary Table

The wind tunnel is also equipped with a Velmex Rotary table and will be used to control the angles of attack of the incoming uniform flow. Mounting the rotary table to the wind tunnel required to machine parts on the milling machine that would join a strut beam and the rotary table, as well as to fix it to the wind tunnel. The rotary table will be controlled by LabVIEW simultaneously while the wind tunnel is running and gathering data

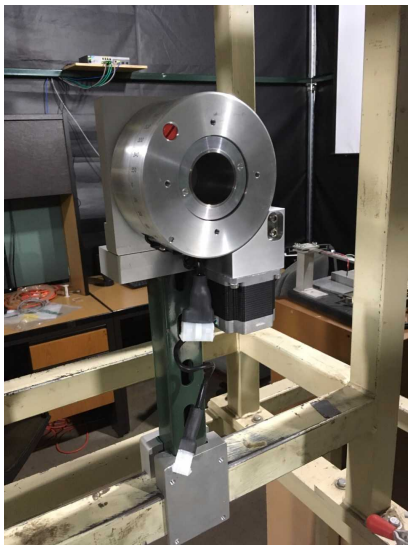

Figure 18: Velmex Rotary Table

.

Experimental Setup

Milling and CNC

Various parts required for the experimentation as well as miscellaneous parts were designed and manufactured via a milling machine. A milling machine is powerful tool for an engineer with designs in mind, since one can easily make a prototype with the proper knowledge of operating such machine. Mounts for the airfoil, pressure transducers, ATI F/T transducers and rotary table were done via a milling machine as well the pitot probe rake used to hold six pitot probes in place for testing wakes behind aerodynamic bodies. Knowing the spindle speed and feed rate of the required work material is crucial for the safety of the user, since operating at wrong speeds can lead to damage to the end mill cutter, the work piece and might injure the user. An end mill is a cutting tool used in any milling machine, and come in different diameters. There are also various types of end mills for example, flat end mill, ball end mill and more.

Figure 19: ¾ inch Flat End Mill, ¾ inch Dove Tail End Mill and ¼ Regular Thread Tap

These are used depending on the surface finish or type of contour desired for the piece. Most of the end mills used in the experimental setup consisted of two flute or two cutting teethes, that work perfectly with aluminum stock material. There are end mills with up to six flutes that are mainly

used in stainless steel or steel in general. A rule of thumb when considering an end mill cutting flute number is to think if one wants to eat material swiftly or at a slower pace, since the lower the flute count the more material is taken away as whereas a higher flute cuts a finer chip and results in a better surface finish. Two fluted end mills are commonly used on aluminum material since it's a softer material than steel. An automatic version of a milling machine would be a CNC or computer numerical control machine; it was required for various parts as well as for the fabrication of the airfoils.

Figure 20: Support for Airfoils

Figure 21: Various Parts Machined

The University of Texas Rio Grande Valley is equipped with a Fadal VMC CNC machine. The CNC machine plays a major role in fabricating parts that required a complex contour or simply parts with complex geometry; basically, parts with round or curved surface. Operating a CNC requires knowledge in G-codes or the commands for the machine. One is required to design a part, in this case the airfoil. Then one must fix the stock material inside the CNC's bed, this fixture is simply called the holding fixture. Some small parts don't require holding fixture since they can be held to a Vis or clamp inside the CNC. After fixing the material inside, one must generate a G-code via the software MasterCAM or by hand (most efficient). Then the operator or user should zero the home axis of the machine and set tool length matching that of the G-code generated. The final step is to drip feed the G-code to the CNC machine via a RS-232 cable from a laptop to the machine. Drip feed is a process in which the CNC machine reads the incoming G-code, stores a few lines of data, then erases those lines after being executed and repeats the process. This is a convenient way of sending the code to machine, since it doesn't require actual memory to store the data.

Figure 22: Fadal VMC CNC Machine

LabVIEW/MATLAB

Interpreting the data obtained from the pressure transducers and scanner requires the use of LabVIEW and MATLAB. This software are powerful tools for measurements and instrumentation, which enables the use of data acquisition. The process meters mentioned before are connected to a National Instruments DAQ with a 16-bit resolution. The DAQ is connected to a computer which allows the user to gather measurements from the instrumentation. A LabVIEW code was developed in order to efficiently gather data; the code consists of gathering any certain number of samples at any given sampling frequency. It also allows the user to visualize the response of the transducer on the front panel and to save the data in a text or data file format; this is helpful when using MATLAB to analyze the data. A MATLAB code was developed in order to analyze the data from the instrumentation. The code imports the data files created by LabVIEW and stores them into an array of cells; then converted to an N x 1 matrix, where N is the number of samples obtained from the instrumentation. For example, to know the velocity inside the test section at each percentage of duty cycle, the wind tunnel was set to increments of 5 % until reaching 100%. For each percentage, the LabVIEW code was used to record the data from the transducers and save the data into a file, while allowing the user to freely name the file, in our case, the files were name according to the percentage in which the wind tunnel was operating (e.g. 5p.dat, 10p.dat …). Then, the MATLAB code was used to import the data, creating an N *x* 21 matrix, where $N \approx 400{,}000$ and the number of columns representing the percentages from least to greatest. Incorporated in the MATLAB code is also Bernoulli's principle and by simply knowing the pressure difference inside the wind tunnel's test section; it allows for the velocity to be known at each different percentage. LabVIEW is also utilized to control the stepper motor with a simple code developed. The code allows for stepper motor to move at any given distance and increment.

The pressure scanner is also controlled with LabVIEW and came with pre-developed codes and VI's. VI's are technically the building blocks of a LabVIEW code; they function together to develop the necessary code. Ultimately, the pressure transducers, scanner and stepper motor are to be run by the same LabVIEW code simultaneously.

Pitot Probe Rake

As mention before, a pitot probe will be used to measure the wake behind the airfoil or any aerodynamic body. Issues may arise if one considers using one pitot probe for testing, for example, not capturing correctly the wake behind the aerodynamic body. Using only one pitot probe will allow one to capture a single wake profile behind the body. Since the airfoil extends form closely wall to wall, a single wake profile can't really show the actual flow behind the body and thus leading to uncertainties in the data. A pitot probe rake was designed and machined in house facilities with a milling machine. The rake consists of six pitot probes covering a span of 10 inches across the airfoil. Its functionality is like that of a clamp, which holds the pitot probe in position and it tighten by three ¼ hexagonal socket screws. This rake can be connected to the pressure scanner and thus obtain pressure readings for the wakes behind the airfoil. The pitot probe rake's design is such that it can be connected to the stepper motor already present on top of the wind tunnel and hence be controlled by LabVIEW and move it any desire distance vertically.

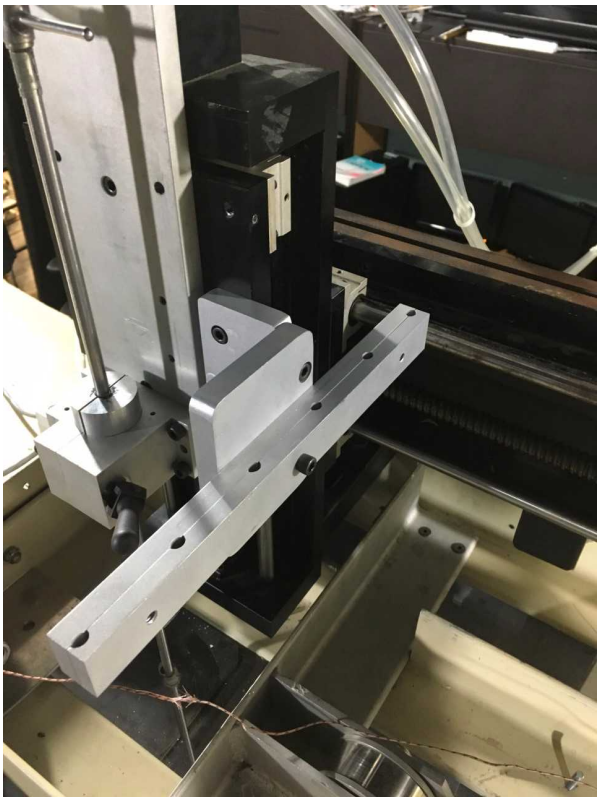

Figure 23: Pitot Probe Rake (Top of Wind Tunnel)

Figure 24: Pitot Probe Rake Holding a Probe

Design & Setup of Airfoils

For the design of the airfoils, the NACA $63_{(4)}$-021 and NACA 0010 cross-sections were used, because it resembles that of the humpback whale pectoral fin, the NACA 6-series are known for their laminar flow characteristics and for manufacturing constraints. The airfoils consist of cast aluminum and 6061-T6 aluminum, and were manufactured by a programmable CNC machine; aluminum facilitates the machining process due to its material properties.

Figure 25: NACA 63(4)-021 Airfoil Profile

Designing the airfoils required for the CAD models to represent something physically possible to machine, as sometimes a CNC machine can't take certain dimensions, especially in the order of 1/50 of an inch when it comes to thickness. Therefore, it was ensured that the CAD models contained realistic, feasible dimensions. Holding the stock material inside the CNC required the use of a holding fixture. This fixture ensure that the bed of the CNC isn't damaged by the end mill cutter. A typical plate of aluminum the size of the bed of the CNC is used when machining a piece whose lower surface is flat; this was the case when machining the first surface of the airfoil. To accommodate for the already machined curved surface of the airfoil, special holding fixtures were machined with the curvature profile of the airfoil, this allowed the opposite un-machined side to

be parallel or squared to the bed of the CNC. The special holding fixtures were machine inside the CNC machine.

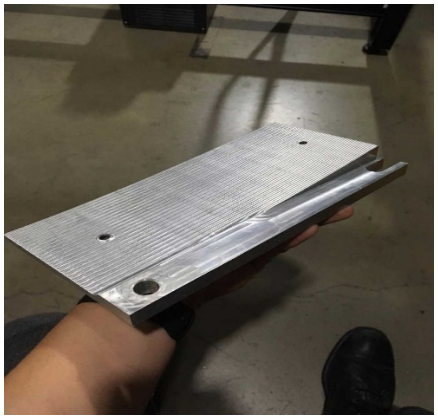

Figure 26: Special Holding Fixture

To facilitate the process of conducting research and experiments, the airfoil was designed in way where one can easily interchange the leading edge of the airfoil to test different geometries. This was done by first designing a body for the airfoil and ensuring that where the surface of the leading edge meets with the surface of the body must be tangential to one another. To join both pieces together, a dove tail connection was implemented to design; the body as the female connection and the leading the edge as the male connection.

Figure 27: Dove Tail Connection

Making the dove tail connections required the use of a special dove tail end mill; it cuts out the shape of the dove tail. One must ensure that the cut is made precise since it can lead to problems once joining both pieces together. To calculate the aerodynamic forces on the surface of the airfoil, pressure tabs were implemented into the CAD model design. This required for that for some portions of the airfoil to be hallow, with channel-like structures allowing the use of Tygon tubing for the 16 different ports on the pressure scanner. Pressure tabs were design on the surface with a diameter of 1/16 inch, placed at 2% of chord length by 4% of span wise direction. A chord length of 8.00 inches (0.204 m) and span of 24 inches (0.610 m), which spans entirely across the test section, were chosen for the NACA 6-serires and a chord length of 14.00 inches (0.356 m) and span of 18 inches (0.457 m) were chosen for the NACA 0010. To neglect the 3-dimensional effects of cross-flow, for example the wing tip vortices; spanning the airfoils across the wind tunnel from wall to wall will ensure 2-dimensional phenomena. The NACA 0010 was design such that it could accommodate for two force and torque transducers, which takes about 6 inches from the span length across the test section. Mounting the NACA 0010 airfoil to the wind tunnel required for various parts to be machined, for example a mounting and tooling interface plate that go on the ATI F/T transducers. Also, a mounting plate was machined to join the rotary table with the airfoil and transducers. These parts are joined by stainless steel rods. As the span wise length suggests, the NACA 0010 doesn't extend from wall to wall inside the test section. To ensure the proper reading s of a two-dimensional phenomenon, measures are to be taken relative close to the center of the airfoil.

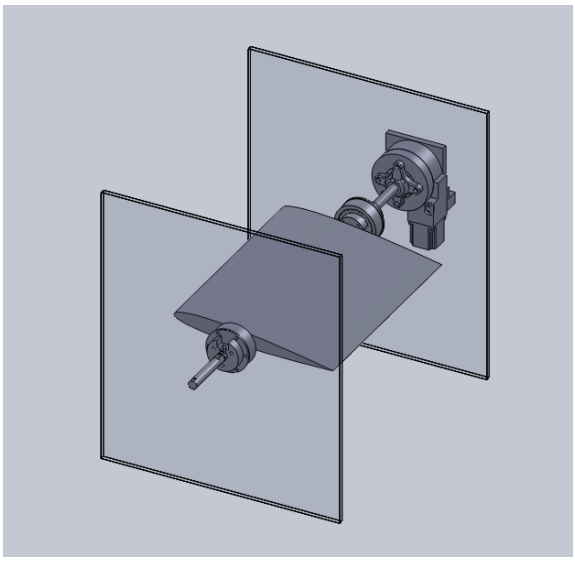

Figure 28: Depiction of Airfoil inside Wind Tunnel

The Reynolds number was calculated with the chosen chord lengths and a freestream velocity of 22.5 m/s (about 50% of wind tunnel), the parameters yielded a Reynolds number of about 303,750, in accordance with the literature published by different sources. For the design of the sinusoidal leading-edge bumps, a sine function was used (e.g. *Asin(xt)*); with a configuration that doesn't extend the chord length but rather constantly changes the chord, while keeping the maximum chord lengths at 8.00 inches and 14 inches. It was found that any of the two configurations doesn't change the results of the tests and both are safe to use []. Amplitudes of 6% and 12% of chord length were used due to that fact that it was observed that smaller bumps tend to result in a higher maximum lift coefficient; as for the larger amplitudes, they result in more gradual delay of stall but lower maximum lift coefficient. The wavelength was taken at 25% of chord length, which yields about eight bumps spaced out evenly across the leading edge, as for the effect of the wavelength on the flow, it was observed there was no apparent affect but it is suggested there is optimal amplitude-to-wavelength.

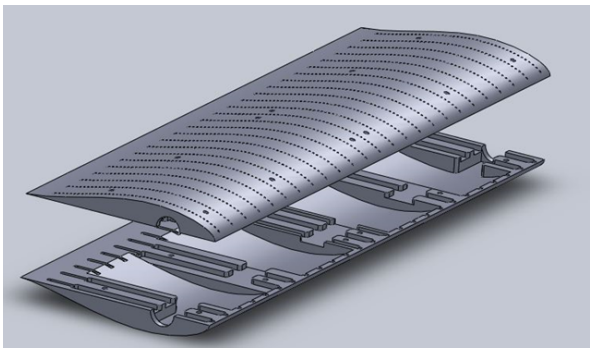

Figure 29: NACA 63(4)-021 airfoil without tubercles

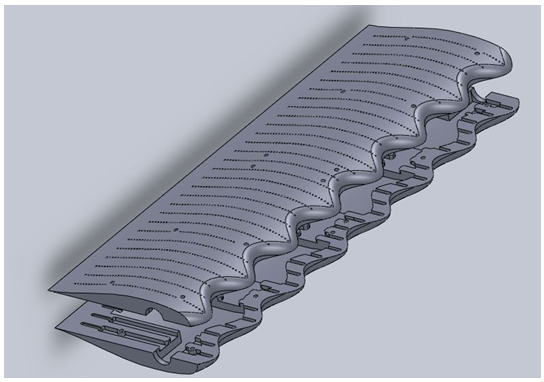

Figure 30: NACA 63(4)-021 airfoil with leading edge tubercles

Figure 31: NACA 0010 Airfoil

VII: APPENDIX-C PRELIMINARY AERODYNAMIC MODEL

THEORECTICAL ANALYSIS

Aerodynamic Model

Establishing Geometry

Obtaining an aerodynamic model for the humpback pectoral fin resulted in a complex and challenging methodology that required the knowledge of theory of functions of complex number, thin-airfoil theory, and Fourier series expansions, the following figure describes the nomenclature for the elliptical wing with perturbations on the leading edge.

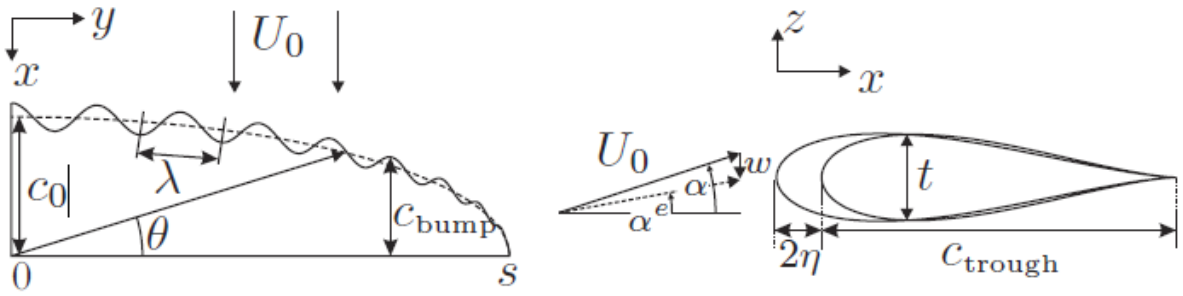

Figure 32: Sketch of the Flipper Geometry

The first step to obtaining such model is to represent the chord as that of an elliptical smooth wing, but with the presence of a perturbation on the leading edge due to the bumps; a Fourier series representation was used to model such geometry, the chord in the span wise direction is defined as follows:

$$c(\theta) = c_0 \sin\theta(1 + \eta S) \tag{3.1}$$

$$S(\theta) = \frac{1}{c_0} \sum_{n=1}^{\infty} a_n \cos(n\theta) \tag{3.2}$$

$$\eta = amplitude\ of\ bumps \tag{3.3}$$

Determining the (a_n) constants in equation (3.2) will all yield the desired perturbation on the leading edge, readily done by the use of a Fourier series expansion. Assume any type of function that resembles that of the tubercles on the humpback whale pectoral fin leading edge; for example, assume S (θ) to be in the form of a decaying sinusoidal exponential or simply a sinusoidal, in the range of (0 to π), this assumption will allow for the solution of the Fourier constant:

$$S(\theta) = \frac{1}{c_0} \sum_{n=1}^{\infty} a_n \cos(n\theta) = \cos(\omega\theta) \tag{3.4}$$

$$a_n = \frac{2}{\pi} c_0 \int_0^{\pi} \cos(\omega\theta)\cos(n\theta) d\theta \tag{3.5}$$

Notice that range of 0 to π corresponds to $-s$ to s of the wing; from the left side tip of the wing to the right-side tip of the wing, thus it is important to note that the half span range is 0 to π/2. After obtaining the constants, it is important to restrict the platform area of the wing, for comparison of various perturbations; this is done by simply by taking the integral from 0 to s, or (0 to π/2).

$$Area = \int_0^s c(y)\, dy = \int_0^{\pi/2} c(\theta)\, s \sin\theta\, d\theta = \frac{4}{\pi} c_0 s \tag{3.6}$$

According to van Nierop et al, this restricts the choices of n and η; in particular, any even value of n will satisfy this condition, regardless of the associated a_n, except for n = 2.

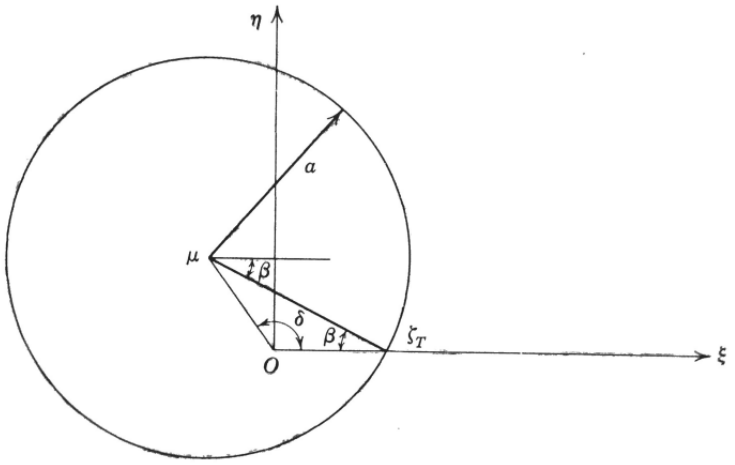

Figure 33: Defining Some Symbols for Flow past a Circle

Function of a Complex Number

Before deriving an expression for the circulation Γ; it is necessary to describe or represent each wing section as that of a Joukowski airfoil; which allows obtaining an analytical expression for the circulation. Theory of functions of complex number comes into action when considering Joukowski airfoils, since such airfoils and its properties are derived from the complex potential, complex velocity and conformal transformation theories. Obtaining a conformal transformation requires that the transformation function be analytical or in others that it is differentiable with respect to a complex number. Differentiability of complex function implies its continuity and guarantees that the function can be differentiated and integrated any number of times. For a complex function to be analytical it must always meet the Cauchy-Riemann conditions. Consider a circle in the *ζ-plane*, placed in a freestream velocity at an angle of attack (Figure 33), the function describing the circle, and its corresponding complex potential and velocity are as follows:

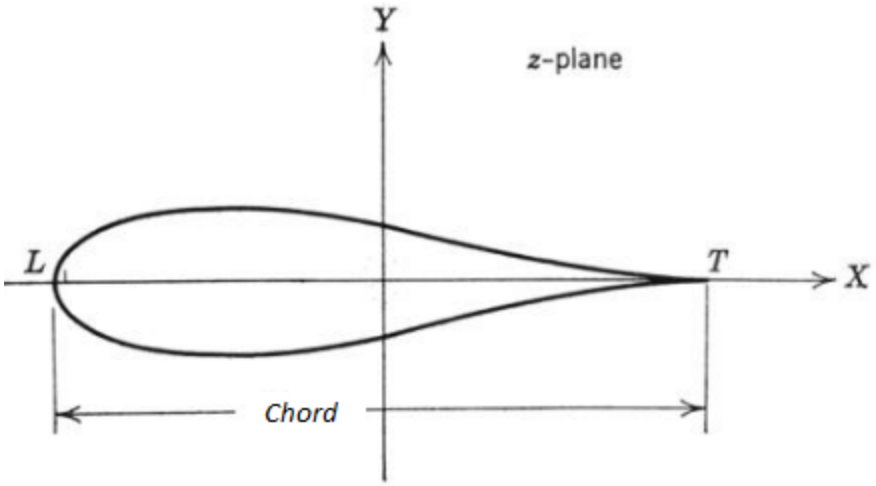

Figure 34: Symmetric Joukowski Airfoil

$$\begin{aligned}\zeta &= ae^{i\gamma} - m \\ &= (r+\lambda)e^{i\gamma} - \lambda\end{aligned} \tag{3.7}$$

$$z = \zeta + \frac{r^2}{\zeta} \tag{3.8}$$

$$F(\zeta) = U_\infty\left[(\zeta-\mu)e^{-i\alpha} + \frac{a^2}{\zeta-\mu}e^{i\alpha}\right] + i\frac{\Gamma}{2\pi}\ln\frac{\zeta-\mu}{ae^{i\alpha}} \tag{3.9}$$

$$W(\zeta) = U_\infty\left[e^{-i\alpha} + \frac{a^2e^{i\alpha}}{(\zeta-\mu)^2}\right] + i\frac{\Gamma}{2\pi}\frac{1}{\zeta-\mu} \tag{3.10}$$

Equation (3.8) is the conformal transformation function describing the Joukowski airfoil in the *z-plane* Figure 3.3. Notice (3.7), "*a*" corresponds to the radius of the circle, but since the leading-edge is being modified, then $a=(r+\lambda)$ where λ is a small perturbation due to the bumps on the leading-edge, if no perturbation is present, then (3.7) would yield the classical Joukowski airfoil. Applying the Kutta condition, which requires that on the circle the complex velocity, be zero at the point that corresponds to the trailing edge (ζ_T). In order words ζ_T is a stagnation point on the airfoil, this point can also be seen in Figure 33. The Kutta condition allows to set (3.9) to zero, hence the circulation can be derived be isolating the circulation term from the rest of the terms and

by some manipulations. Thus, the expression obtained for the circulation by applying the Kutta condition is:

$$\Gamma(\theta) = -4\pi a U_\infty \sin(\alpha + \beta) \tag{3.11}$$

$$\Gamma(\theta) = -4\pi(r + \lambda) U_\infty \sin(\alpha^e) \tag{3.12}$$

And by expanding the following,

$$\sin(\alpha^e) = \alpha^e + O((\alpha^e)^3) \tag{3.13}$$

$$4(r + \lambda) = c_0 \sin\theta(1 + T + \eta S) \tag{3.14}$$

Then, the circulation can be expressed as,

$$\Gamma(\theta) = -\pi c_0 U_\infty \sin\theta(1 + T + \eta S)\alpha^e \tag{3.15}$$

Where,

$$T = \frac{4}{3\sqrt{3}} \frac{t_0}{c_0} \tag{3.16}$$

$$S = \frac{1}{c_0} \sum_{n=1}^{\infty} a_n \cos(n\theta) \tag{3.2}$$

Notice from (3.11) and (3.12) that the angle of attack is represented as the effective angle of attack; this is since ultimately, the expression obtained for the circulation will be applied to a wing and thus the effective angle of attack needs to be considered at each cross-section of the wing. Also, (16) ensures that the thickness ratio is constant across the span wise direction.

Prandtl's Lifting Line Model

Now that the circulation is fully defined (3.15), the next step is to precede to the three-dimensional small-disturbance solutions, in this case the lifting-line model, which is represented by the following equation:

$$\frac{-2\Gamma(y)}{m_0(y)c(y)U_\infty} - \frac{1}{4\pi U_\infty}\int_{-s}^{s}\frac{[d\Gamma(y_0)/dy]dy_0}{y-y_0} + \alpha(y) - \alpha_{L0}(y) = 0 \tag{3.17}$$

This equation can also be seen as the combination of the angles, as described from the following,

$$-\alpha_e - \alpha_i + \alpha - \alpha_{L0} = 0 \tag{3.18}$$

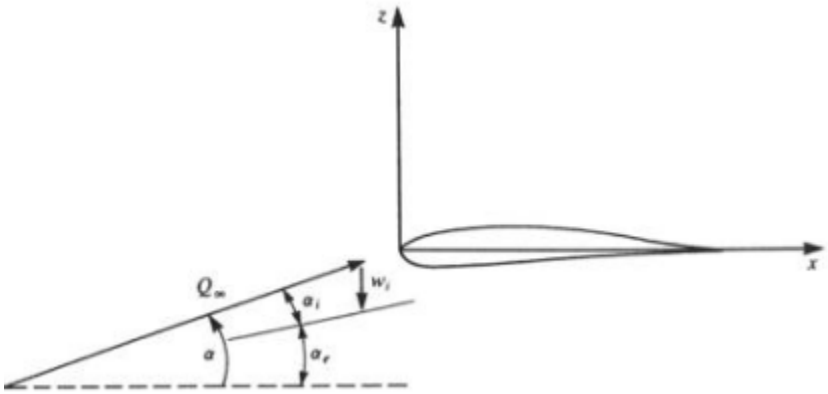

Figure 35: Two-Dimensional Section of a Three-Dimensional Wing

From (3.17) and (3.18), α_i is the induced angle due to the downwash; $\alpha(y)$ is the local angle of attack relative to U_∞ and $\alpha_{L0}(y)$ is the airfoil section zero-lift angle. Note that geometric twist occurs for a span wise variation of the angle of attack, while aerodynamic twist occurs for a span wise variation of the zero-lift angle. By using (3.15) and (3.17), one can solve for the lift and induced drag of the wing by using the Kutta-Joukowski theorem in the *y-plane* or the span wise direction; the lift and induced drag are given by the following:

$$L = \rho U_\infty \int_{-s}^{s} \Gamma(y)\,dy \tag{3.19}$$

$$D_i = -\rho \int_{-s}^{s} w_i(y)\Gamma(y)\,dy \tag{3.20}$$

$$w_i(y) = \frac{1}{4\pi}\int_{-s}^{s}\frac{[d\Gamma(y_0)/dy]dy_0}{y-y_0} \tag{3.21}$$

As it can be seen, the only unknown in these set of equations is the circulation $\Gamma(y)$; this is when (3.15) comes into play; the only problem is that variation of the effective angle of attack is also

unknown. To solve for the unknown variation; a Fourier series expansion was used to generalize the effective angle of attack. Let the effective angle of attack be represented by,

$$\alpha^e = \sum_{m=1}^{\infty} A_m \sin(m\theta) \tag{3.22}$$

Consequently, the circulation is also expressed as a Fourier series expansion,

$$\Gamma(\theta) = -\pi c_0 U_\infty \sin\theta (1 + T + \eta S) \sum_{m=1}^{\infty} A_m \sin(m\theta) \tag{3.23}$$

Notice that equation (3.23) fulfills the condition at the wingtips (0 and π) where the pressure difference must reduce to zero, which implies that the circulation must also be zero as well. Substituting (3.23) into (3.17) and by using the Glauert integral identity, the following expression was obtained:

$$\sum_{m=1}^{\infty} A_m \frac{\sin(m\theta)}{\sin(\theta)} \left[\frac{(1 + T + \eta S)}{(1 + \eta S)} + \frac{c_0 \pi}{4s} (1 + T + \eta S) m \right] = \alpha(\theta) - \alpha_{L0}(\theta) \tag{3.24}$$

Where,

$$\frac{c_0 \pi}{4s} = \frac{2}{AR} = \frac{2}{Aspect\ Ratio} \tag{3.25}$$

Equation (3.24) will act as the governing equation for the coefficients in the circulation distribution, also as a remark; the aspect ratio of an elliptic wing appeared in (3.24) after some simplifications to the equation. Solving for the coefficients in equation (3.24) is done by noticing that the right-hand side of the equation is simply a Fourier series representation; a MATLAB code will be implemented to solve for such coefficients and thus the circulation across the wing.

RESULTS: Geometry of Wing and Lift

After solving for the Fourier series expansion of the assumed function representing the tubercles on the wing; the following results were obtained for the geometry of the aerodynamic model (s=3.6 m). Shown on Figure 36 is the calculated geometry of the wing.

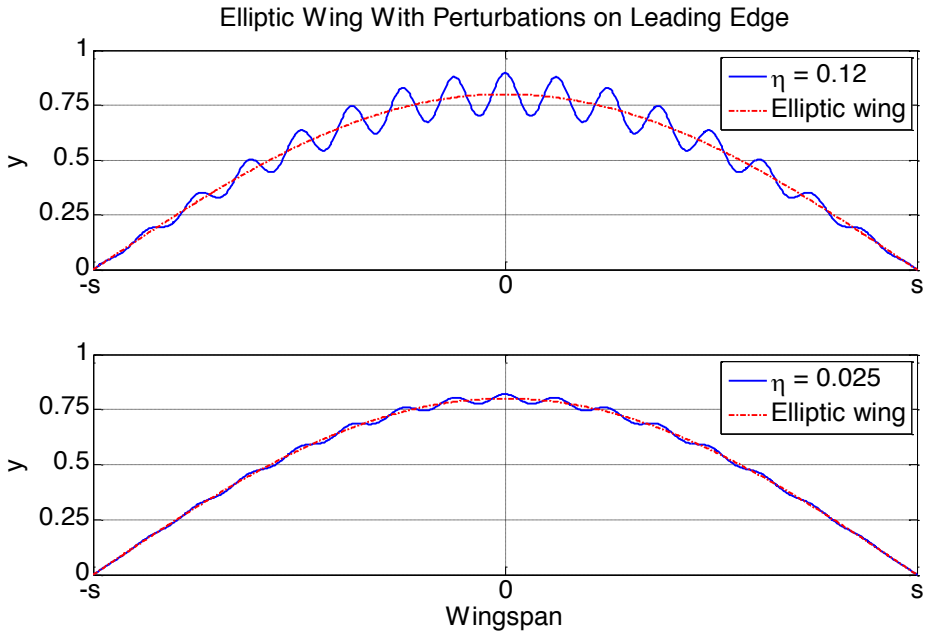

Figure 36: Geometry Obtained for the Flipper

By simply changing the η parameter representing the amplitude of the bumps one can obtain different geometries for the wing. Also by assuming other functions representing the geometry of the wing, other shapes can be obtained. The solution for the circulation expression was obtained by solving for the constants of the expansion by means of numerical methods.

$$A_n = \frac{2}{\pi}\frac{1}{G_j}\int_0^{\pi} \alpha(\theta)\sin(\theta)\sin(n\theta)d\theta \tag{4.1}$$

$$G_j = c_j(1+T+\eta S)\left[\frac{1}{c_o(1+\eta S)} + \frac{n\pi}{4s}\right] \tag{4.2}$$

$$c_j = c_o \sin(\theta_j) \tag{4.3}$$

The subscript *j* on (4.1) and (4.2) represents the intervals taken to section the wing and thus allowing to solve numerically for the Fourier constants for a given section of the wing. This was done via an implementation of a MATLAB code. Unlike van Nierop et al. where it wasn't clear the methodology for obtaining a solution for their circulation expression, van Nierop et al. utilized a Chebyshev series expansion as well as a perturbation method. A simple Fourier series expansion was used for this aerodynamic model; even though a Chebyshev series can give a better insight of the problem. After obtaining a solution for the Fourier constant, it can be substituted back to the circulation expression and hence to the Kutta-Joukowski theorem to obtain the lift on the wing. Sketched on Figure 37, is the circulation distribution across the wing, where the largest magnitude is located approximately at the midpoint between the wing root and wing tip for both sides. This magnitude suggests that most of the aerodynamic loadings will be located at that point. Represented by the different color line marks; Figure 37 also shows how the circulation is varying with increasing angle of attack. As anticipated, the circulation tends to increase with increasing angle of attack. Calculation of the lift force and lift coefficient are sketched on Figure 38, notice that the slope of the curve remains linear with increasing angle of attack, again this due to the fact

that the solution is for the ideal case of the fluid and thus no effects due to viscosity can be predicted.

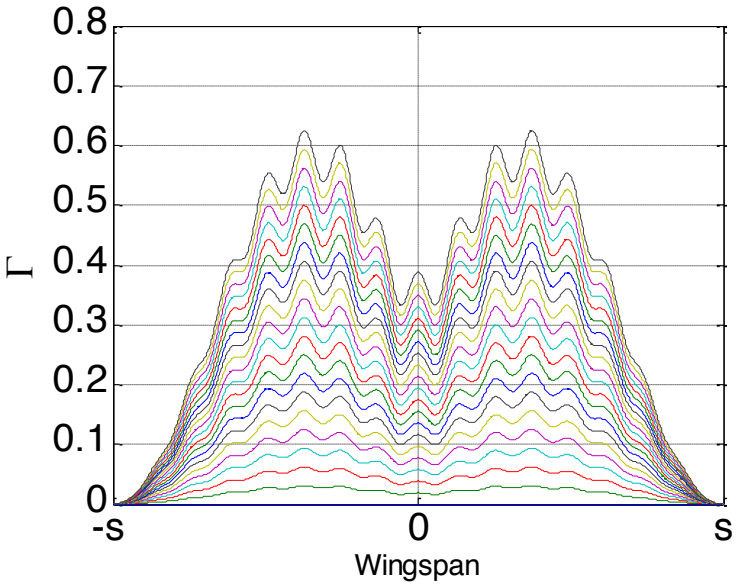

Figure 37: Circulation Distribution across the Span of the Wing for Various Angles of Attack

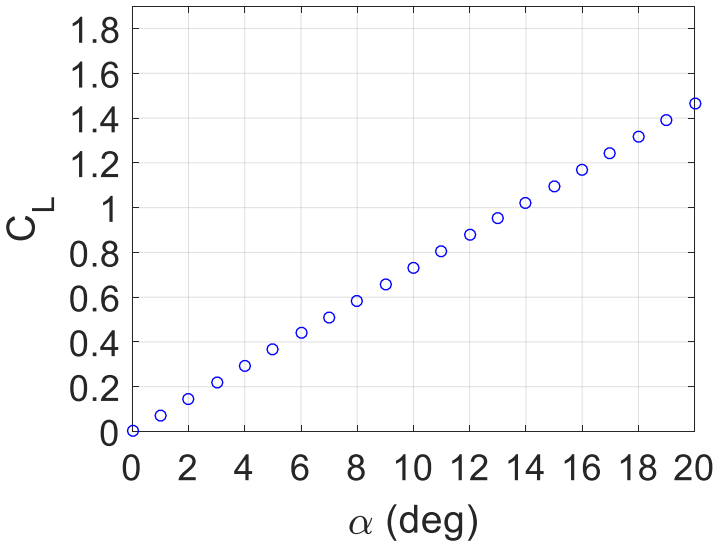

Figure 38: Lift Coefficient vs. Angle of Attack

Pressure Distribution and Separation Points

After solving for the Fourier constants and obtaining a solution for the circulation, one is able to solve for the complex velocity and hence the pressure distribution on the surface of the Joukowski airfoil. From theory, the velocity on the surface of the airfoil is obtained by the following:

$$W(z) = W(\zeta)\frac{1}{dz/d\zeta} \tag{4.4}$$

$$\frac{dz}{d\zeta} = 1 - \frac{r^2}{\zeta^2} \tag{4.5}$$

By substituting equation (3.7) and the expression for circulation into equation (3.10), the following complex velocity on the circle is obtained.

$$W(\zeta) = i2V_\infty[(\alpha^e) - \sin(\alpha^e - \gamma)]e^{-i\gamma} \tag{4.6}$$

From Bernoulli's principle, the pressure distribution on the surface of the Joukowski airfoil is given by:

$$p(x) = p_\infty - \frac{\rho}{2}V_\infty{}^2\left[1 - \frac{|W(z)|^2}{V_\infty^2}\right] \tag{4.7}$$

$$|W(z)|^2 = |W(\zeta)|^2\frac{1}{\left|dz/d\zeta\right|^2} \tag{4.8}$$

$$|W(\zeta)| = 2V_\infty[(\alpha^e) - \sin(\alpha^e - \gamma)] \tag{4.9}$$

Notice that in (4.7) the pressure is obtained by using the magnitude of the complex velocity on the surface of the airfoil, consequently (4.6) takes the form of (4.9). Equation (4.9) is key into demonstrating the effects of the bumps on the wing, due to the presence of the effective angle of attack in the equation. As mention before, Equation 1.7 implies that the variation of the chord and thickness along the wing causes a variation in the circulation Γ. Such span wise changes in the circulation generate a sheet of stream wise vortices behind the wing, which causes a downwash (w) at each cross section of the wing and thus vary the effective angle of attack along the span.

$$\alpha^{e} = \alpha - \frac{w}{V_{\infty}}$$

At this point of the aerodynamic model, assumption of inviscid flow has been established for the most part of the equations. But to properly model the stalling characteristics of the wing at different configurations of bumps; one must employ the knowledge of boundary layer theory, an exclusively viscous phenomenon. Even by looking at Figure 38, inviscid theory suggests that the lift coefficient keeps increasing linearly with increasing angle of attack. In real life, this is not the case since with increasing angle of attack the wing will eventually reach a maximum lift coefficient and then undergo through stall or losses in the lift. The reason for this is that when a wing is under stall, pressure drag is also tremendously increased and frictional forces dominate most the surface of the wing, causing the flow to be almost entirely separated and turbulent. Inviscid theory fails to represent the stalling characteristics of wings; therefore, turbulent boundary layer theory is used to identify the position of the flow separation while undergoing stall. Stratford's method for predicting separation is employ; the advantage of this method is that, it does not require detailed

knowledge of the flow in the boundary layer. Stratford's criterion for separation, which gives best all-around agreement with experimental results, is as follows:

$$F(x) = C_p \left(x \frac{dC_p}{dx} \right)^{1/2} \left(10^{-6} \, \mathrm{Re}_x \right)^{-1/10} \tag{4.11}$$

$$Cp = \frac{p(x)}{1/2 \rho V_\infty^2} \tag{4.12}$$

$$\mathrm{Re}_x = \frac{V_\infty x}{\nu} \tag{4.13}$$

If the maximum value of *F(x)* is greater than 0.40, then separation is predicted when *F(x)* = 0.40. If the maximum value lies between 0.35 and 0.40, separation occurs at the maximum value. If the maximum value is less than 0.35, then separation does not occur. The only thing left is to identify the *x* location where each cross section of the smooth and bumpy elliptic wing is stalling. To calculate where the bumpy wing is stalling, it is assumed that for any cross section of the bumpy wing where the *x* location is less than that of the smooth wing, then that cross section is stalled. Sections stall independently of neighboring sections, which is reasonable in the long-wavelength limit since the flow is then predominantly chord wise and the cause of separation or stall will be the upstream flow rather than the flow in neighboring sections. Total lift on a partially stalled wing is computed by summing the lift at each cross section, where stalled sections contribute through the vertical component of the form drag or pressure drag. This procedure will replicate the results as shown by van Nierop et al. The following figure shows the obtained pressure distribution on a bump and trough. The obtained pressure distribution resembles that from that from published

papers and shown in Figure 39 is the comparison between the obtained distribution and van Nierop et al. respectively. Figure 39 also suggests that a larger adverse pressure gradient is present on the trough than the bump, implying that stalling occurs first in the troughs and at a lower angle of attack.

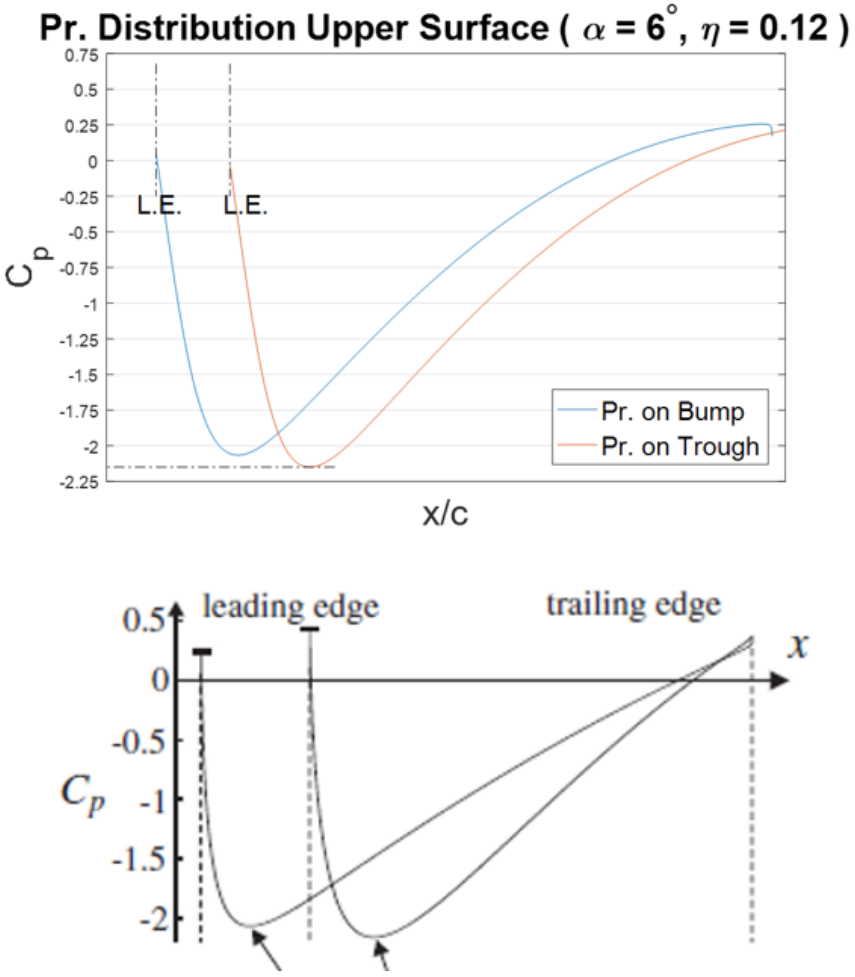

Figure 39: Comparison of Obtained Pressure Distribution